Investigation of the Flow Structure of Single- and Dual-Celled Tornadoes and their Wind Effects on a Dome Structure

Tiantian Li¹, Guirong Yan*¹, Ruoqiang Feng² and Xiaoyong Mao³

Abstract

Due to the incredible property loss and significant fatalities induced by tornadoes each year, tornado research has attracted considerable attention. However, previous studies mainly focused on the wind characteristics of tornadoes with the single-cell flow structure, and only a few targeted tornadoes with the dual-cell flow structure. In addition, the influence of flow structure of the tornado on its wind effects has not been sufficiently explored. This study is therefore aimed to investigate how the number of cells in the flow structure affects the wind effects acting on civil structures through Computational Fluid Dynamics (CFD) simulations. The paper is focused on the single-cell and dual-cell flow structure, both of which belong to the category of single-vortex tornadoes. For completeness, the wind characteristics of both types of tornadoes are also studied and compared. The applied CFD simulation strategies are verified based on a real-world tornado. The obtained results show that, due to the central downdraft in the dual-celled tornado, its turbulence intensity is higher than that of the singlecelled tornado. The pressure profile for the dual-celled tornado has a wide, flat distribution, while the corresponding profile for the single-celled tornado has a narrow, single peak. The two drag forces induced by the single-celled tornado follow a typical trend, i.e., they reach their peak values when the dome center moves to the tornado core radius, while the corresponding variations under the dual-celled tornado tend to be more random. Similar observations can be found from the two overturning moments. This suggests that the wind loading induced by the dual-celled tornado is more dynamic than that induced by the singlecelled tornado.

Keywords: tornado; flow structure; dual-celled; single-celled; wind effects

E-mail address: yang@mst.edu

¹Department of Civil, Architectural and Environmental Engineering, Missouri University of Science and Technology, 1401 N. Pine St., Rolla, MO 65409

²School of Civil Engineering, Member of the Key Laboratory of Concrete and Prestressed Concrete Structures of Ministry of Education, Southeast University, Nanjing, China

³School of Civil Engineering, Suzhou University of Science and Technology, Suzhou, Jiangsu, China

^{*} Corresponding author. 331 Butler-Carlton Hall, Department of Civil, Architectural and Environmental Engineering, Missouri University of Science and Technology, 1401 N. Pine St., Rolla, MO 65409, USA.

1. Introduction

In recent years, tornadoes have become a significant cause of injury, death, and property damage. On average, they cause \$10B of property loss each year in the United States. Tornadoes are violently rotating columns of air that extend from a thunderstorm to the ground. They can generate intense winds at the speed of up to 135 m/s or 302 mph [1]. Due to the violent nature and unpredicted path of tornadoes, it is very challenging to obtain the in situ measurements of tornadoes, especially near-ground measurements [2]. Therefore, to characterize tornadic wind fields and to study tornado-induced wind effects on civil structures, researchers developed analytical models and simulated tornadoes using laboratory tornado simulators and Computational Fluid Dynamics (CFD) simulations.

Analytical modeling of tornadic wind flow has first been applied to investigate flow characteristics of tornado vortices. Several analytical models have been developed. The mathematical expressions of some representative analytical models are listed in Table 1. Rankine vortex model only defined tangential velocity (V_t) in the flow [3], as shown in Table 1. This model divided the vortex into two parts: the inner part of the vortex in which V_t linearly increased with the radial distance and the outer part of the vortex in which V_t was a decreasing function of radial distance in hyperbolic form. The changeover from linear to hyperbolic form of V_t profile created a sharp pinnacle at core radius (designated as R_c , which was the radius where the maximum tangential velocity $(V_{t,max})$ occurred. Later on, Rankine model was modified by Deppermann [4]. A single equation was used to represent the vortex, and the sharp pinnacle at R_c observed in Rankine model was smoothed out. Then, a more advanced model (Burgers-Rott vortex model) was developed [5, 6], which defined all three wind velocity components (Tangential velocity V_t , Radial velocity V_r , and Axial velocity V_{ν}) to better capture the wind characteristics of tornadoes. However, almost all the previous analytical models pertain to single-celled single-vortex tornadoes except the following. An analytical model (Sullivan model) of a dual-celled tornado was proposed [7], and its mathematical expression is also listed in Table 1. In the flow generated by this model, V_r and V_v reversed their directions around the tornado center, generating a central recirculation pattern that was absent in the single-celled tornado. However, in this model, V_r grew without limits, which was not consistent with the real-world situation. Later on, a new model (Vatistas model) was reported for intense vortices [8], as shown in Table 1, which was able to produce a dual-celled tornado by a proper selection of the scaling constants, e.g. $\kappa=1.1, \ \eta=0.625$, and $\beta=0.6$. In this model, the velocities were bounded. It was shown that V_r profile along a radius exhibited a direction reversal near the tornado center when a dual-celled tornado appeared. Burgers-Rott model [5, 6] was employed to generate a single-celled vortex and Sullivan model [7] to generate a dual-celled vortex to investigate the effects of different flow structures on the basic characteristics of tornado vortices [9]. Recently, Manikis extended the work of Vatistas [8] to consider the time effect, decaying of vortices, on the dualcelled tornadoes [10].

Table 1. Mathematical expression of analytical tornado models

Vortex model	Radial velocity (V_r)	Tangential velocity (V_t)	Axial velocity (V_v)
Rankine model	0	$\frac{V_{t,max}r}{R_c}, r < R_c$ $\frac{V_{t,max}R_c}{r}, r \ge R_c$	0
Modified Rankine model	0	$\frac{2rV_{t,max}R_c}{r^2 + R_c^2}$	0
Burgers-Rott model	-ar	$\frac{\Gamma}{2\pi r}(1-e^{-\frac{ar^2}{2\nu}})$	2az
Sullivan model	$-ar + \frac{6\nu}{r}(1$ $-e^{-\frac{ar^2}{2\nu}})$	$\frac{\Gamma}{2\pi r} \frac{H(\frac{ar^2}{2\nu})}{H(\infty)}$	$2az(1-3e^{-\frac{ar^2}{2\nu}})$
Vatistas model	K	$\frac{C_{\infty}}{r} \int_0^r \left[\frac{1 + \beta r^2}{(1 + \eta \beta r^2)^{(1/\eta \kappa)}} \right]^m r dr$	$2\alpha z \left[\frac{1}{(1+\eta\beta r^2)^2} - \frac{\kappa}{(1+\beta r^2)^2}\right]$

Note: $V_{t,max}$ denotes the maximum tangential velocity; R_c the core radius, where $V_{t,max}$ is observed; r the radial distance from the vortex center; Γ the strength of circulation; a the strength of the suction; ν the kinematic viscosity; $H(x) = \int_0^x e^{f(t)} dt$, $f(t) = -t + 3 \int_0^t (1 - e^{-y}) \frac{dy}{y}$; α , κ , η , and β are scaling constants, $\alpha = \frac{2\eta\beta}{R_e\kappa}$; $C_\infty = 1/\int_0^\infty \left[\frac{1+\beta r^2}{(1+\eta\beta r^2)^{(1/\eta\kappa)}}\right]^m r dr$; $m = \frac{\alpha\kappa R_e}{2\beta}$, R_e is the Reynolds number.

Besides analytical modeling, experimental simulations also play an important role in generating essential features of real-world tornadoes. Ward developed the first laboratory tornado simulator and simulated single-celled tornadoes [11]. He investigated the influence of the aspect ratio on R_c and surface pressure profile. Later on, extensive laboratory simulations were conducted through the updated Ward-type simulators, and different aspects regarding tornado flow characteristics were investigated [12-17]. For example, various tornado-like vortex configurations were generated as a function of swirl ratio (S), radial Reynolds number (R_{e_r}) , and aspect ratio, including a single laminar vortex, a single vortex with breakdown, and multiple vortices [12, 13]. V_r and V_t as well as R_c of the tornado increase with the increase of S [13, 16]. The influence of tornado translation [14] and surface friction [15] on the wind field were also studied. Tornado translation caused a local increase in S and increased R_c compared to a stationary vortex. Surface friction made the flow more turbulent and thus caused greater eddy exchange of momentum. In addition to the Ward-type tornado simulator, tornadoes have been simulated and studied in two other types of laboratory tornado simulators at Iowa State University [18] and Western University [19] to characterize tornadic wind fields [20-23]. During the simulations in the Ward-type laboratory tornado simulator at Texas Tech University, the transition of the flow structure from a single-cell to a dual-cell with the

increase of S was observed [24, 25]. It was found that the aspect ratio not only affected R_c of both single- and dual-celled tornadoes but also S at which the critical transition occurred. It also showed that the Burgers-Rott model [5, 6] closely fitted the averaged V_t profile of the single-celled tornado generated in the laboratory tornado simulator, and the Sullivan model [7] fitted the dual-celled tornadoes produced in the lab very well.

In addition, CFD simulations have been applied to numerically simulate the different types of laboratory tornado simulators, including Ward-type tornado simulator and tornado simulators at Iowa State University and Western University, to investigate the generated tornado vortices and the airflow through these tornado simulators [26-30]. Among these studies, Ishihara et al. [26] simulated a Ward-type tornado simulator and investigated both single- and dual-celled tornadoes regarding the mean velocity field and pressure field. It was found that a single-celled tornado appeared when S is low and V_{ν} showed peaks at the tornado center; and that a dual-celled tornado appeared when S is high and $V_{t,max}$ appeared near ground.

Based on the understanding of the tornado vortex itself, the tornado-induced wind loading effects and its static impact (mean aerodynamic wind loading) on civil structures have then been investigated [18, 28, 31-36]. A few attempts have also been made on the study of non-stationary characteristics of tornadoes. Dynamic wind pressure on a low-rise building frame was studied through laboratory tornado simulations and the results showed that the characteristics of dynamic pressures were strongly affected by the relative location of the structure to the tornado and were very different from those under straight-line winds [37]. Transient wind loads on a cubic building under a translating tornado were investigated in a laboratory simulator [38] and through CFD simulations [39]. In addition, tornado-induced wind loads on a low-rise gable-roofed building were explored with respect to swirl ratio, translation speed, and building parameters [40].

According to the comprehensive literature review, previous studies were mainly focused on the characterization of the wind field induced by either single-celled or dual-celled tornadoes, and little if any research is about the comparison on the wind characteristics between single- and dual-celled tornadic wind fields. Tang et al. [25] and Ishihara et al. [26] have compared single- and dual-celled tornadoes through laboratory and numerical tornado simulations, respectively, but their emphases were primarily on the mean velocity field and pressure field, and they did not compare and discuss the characteristics of turbulence in the two tornadic wind fields and the tornado-induced wind effects on civil structures. However, turbulence can significantly affect the wind flow around civil structures and aerodynamic force; and can produce significant dynamic effect on some types of civil structures. To fill this research gap, in this study, CFD simulations will be employed to systematically investigate the differences between single- and dual-celled tornadoes regarding the wind characteristics and the induced wind effects on civil structures. The remainder of this study is organized as follows. First, the civil structure of interest, a dome structure, will be introduced. The CFD simulation setup for generating a single-celled tornado and a dual-celled tornado will be described. Second, the verification of the applied CFD simulation strategies will be demonstrated by comparing the simulated results to radar-measured data of a real-world tornado. Third, the wind characteristics of the two types of tornadoes will be investigated and compared, with respect to the flow structure, tangential velocity, turbulence intensity, and static pressure. Lastly, the wind effects on the dome structure induced by these two types of tornadoes will be compared in terms of the wind pressure on the dome surface and the total forces and moments.

2. Simulation of Tornadic Wind Field

2.1 Civil structure considered in this study

The civil structure considered in this study is a Kiewitt-type K6-7 single-layer spherical dome structure, as shown in Fig. 1. Its span is 75 m and its rise is 25 m. 462 tubular beam members form a frame, which is covered by 294 shells.

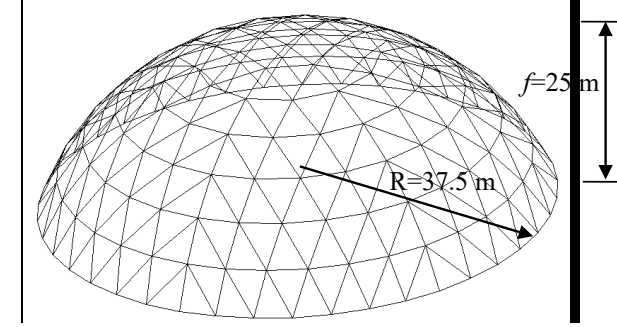


Fig. 1. A Kiewitt-type K6-7 single-layer spherical dome structure.

2.2 Real-world tornado simulated in this study

The simulated tornadic wind field is based on a real-world F4 tornado, the Spencer, SD tornado of May 30, 1998 (hereafter "Spencer Tornado"). From the three-dimensional ground-based velocity track display analysis conducted by Kosiba and Wurman, a dual-celled single-vortex flow structure is maintained for Spencer Tornado throughout their 8-min observation period [41]. Recent research findings also demonstrate the dual-celled vortex structure of Spencer Tornado [42]. $V_{t,max}$ of Spencer Tornado is around 63 m/s, and its R_c fluctuates around 220 m at the elevation of 80 m during the observation period [28]. This tornado will be numerically simulated using ANSYS FLUENT, and parameters will be adjusted to generate tornadoes with different flow structures, i.e., dual- and single-celled flow structures.

2.3 All simulated cases and simulation setup

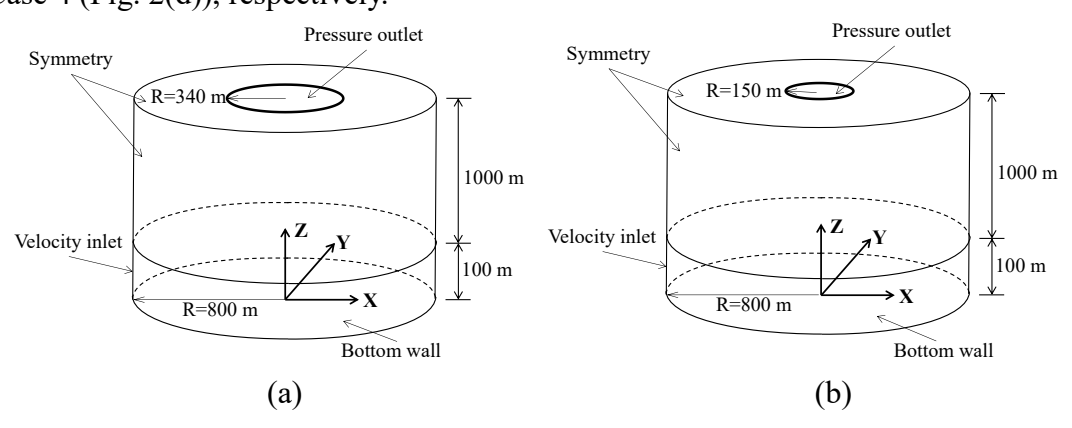
All simulated cases are listed in Table 2. Case 1 is simulated to reproduce Spencer Tornado and to verify the applied CFD simulation strategies. In Case 1, all civil structures are eliminated to simulate the tornadic wind field only; the radius of pressure outlet is set to be 340 m to achieve the dual-celled flow structure. In the real world, most of tornadoes possess the dual-celled flow structure, which normally has a larger core size. Case 2 is targeted to generate a tornado with the single-celled flow structure, which will be achieved by modifying the radius of the pressure outlet in Case 1 to 150 m. Again, no civil structures are present in this wind field. The results from Case 1 and Case 2 will be used to compare the wind characteristics of tornadic wind fields between dual- and single-celled flow structures. In

Cases 3 and 4, the dome structure described in Section 2.1 is placed in the computational domain in order to compare the wind effects on the dome surface induced by tornadoes with different flow structures.

Table 2. All cases simulated in this study.

Cases	Flow structure	With civil structure present?	Radius of pressure outlet (m)
Case 1	Dual-celled	No	340
Case 2	Single-celled	No	150
Case 3	Dual-celled	Yes	340
Case 4	Single-celled	Yes	150

Four different computational domains (Fig. 2) are established corresponding to the four simulated cases. In each case, the computational domain consists of two cylinders to simulate the swirling wind flow. The height of the bottom cylinder is 100 m, resembling the inflow zone. The height of the top cylinder is 1,000 m, resembling the convection zone. The radii of both cylinders are the same, 800 m. The boundary conditions on the inflow surface and on the outflow circle are defined as velocity-inlet and pressure-outlet, respectively. The boundary condition on the ground plane is defined as a no-slip wall when a stationary tornado is simulated and as a moving wall when a translating tornado is simulated. The rest top and side boundary surfaces are defined as symmetric boundary conditions. The main difference in CFD simulation setup between Cases 1 and 2 lies in the radius of the pressure outlet, which are 340 m and 150 m for Case 1 (Fig. 2(a)) and Case 2 (Fig. 2(b)), respectively. The dome structure is not present in these two cases. To investigate tornadic wind loads on dome structures, the dome structure is included in Case 1 and Case 2 to generate Case 3 (Fig. 2(c)) and Case 4 (Fig. 2(d)), respectively.



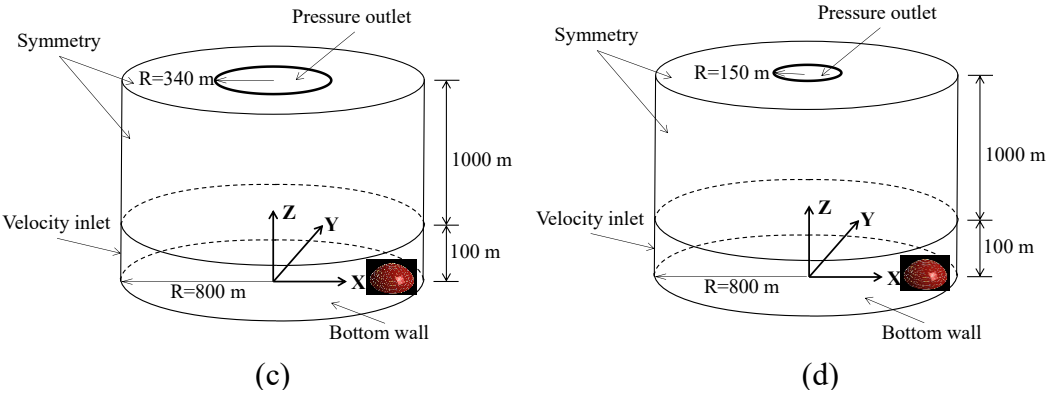


Fig. 2. Computational domains of the simulated tornadic wind fields: (a) Case 1; (b) Case 2; (c) Case 3; (d) Case 4.

For all the four simulated cases, an inflow with tangential velocity (V_t) and radial velocity (V_r) enters the velocity inlet and exits from the pressure outlet. The equations used for V_t and V_r along the height are shown in Eqs. (1)-(2). They are obtained from the radar-measured data only at a location 800 m away from the tornado center through the height of 320 m. More details about the regression equations can be found in [43].

$$V_t = 20.61(\frac{z}{20})^{0.1774} \tag{1}$$

$$V_r = \begin{cases} -31.14 \left(\frac{z}{20}\right)^{0.169}, & z < 20 \text{ m} \\ 45.14 \left(\frac{z}{20}\right)^{0.1826} - 76.48, & z \ge 20 \text{ m} \end{cases}$$
 (2)

where z is the height above the ground.

Pointwise [44] is applied to develop the geometric model of the computational domain. For Cases 1 and 2, only structured mesh is applied. Fig. 3(a) presents the arrangement of the structured mesh deployed in Case 1, and similar arrangement of the meshes is used in Case 2. Fine mesh is applied to the near-ground wind field (the bottom cylinder in Fig. 2(a)), and coarse mesh is applied to higher levels (the top cylinder in Fig. 2(a)). Accurate solution in the desired region and computational efficiency can be achieved at the same time using the combination of the fine and coarse meshes. For Cases 3 and 4, hybrid mesh is applied, including hexahedra, tetrahedra, pyramids, and prisms. Fig. 3(b) presents the arrangement of the meshes applied in Case 3, and similar arrangement of the meshes is used in Case 4. The cuboid (Zone 1 in Fig. 3(b)) containing the dome structure is meshed into unstructured grids (tetrahedron, pyramid, and prism). The remaining zones (Zones 2, 3, and 4) are meshed into structured hexahedral grids. In addition, inflation grid sizing is applied to all the four cases, in order to capture the variations in the wind velocity profile near the ground (boundary layer) more accurately. In Cases 1 and 2, inflation grid sizing is applied to the ground surface; and in Cases 3 and 4, inflation grid sizing is applied to both the ground surface and the dome surface. The thickness of the first layer is 0.002 m and its Y+ value is 250 based on the flat-plate boundary layer theory. In total, 36 layers are applied with the growth rate of 1.2. More details about the mesh strategies can be referred to [43].

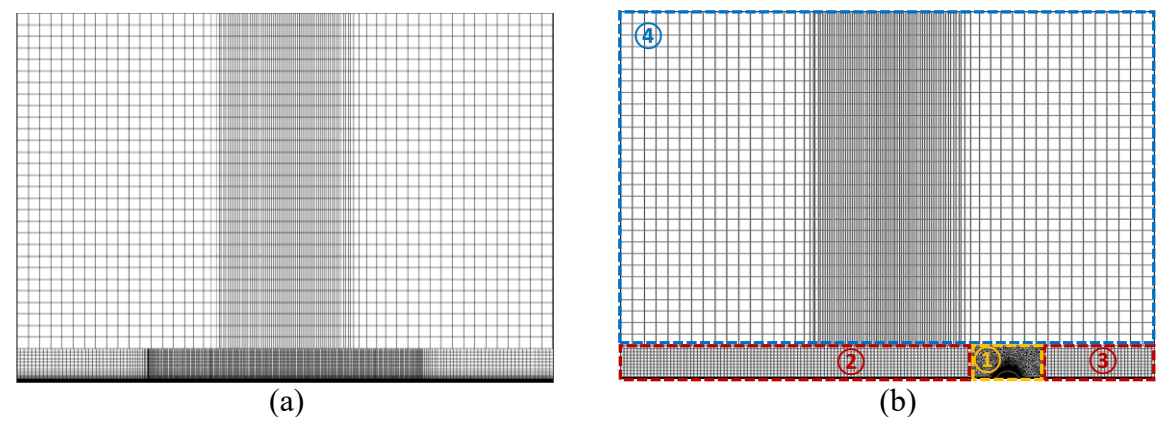


Fig. 3. The arrangement of the meshes on the X-Z plane where Y=0 in the computational domain: (a) Case 1; (b) Case 3.

In the CFD simulations, the tornadic wind field is governed by the filtered time-dependent Navier-Stokes equations. That is, the Large-Eddy Simulation (LES) is applied here to solve large eddies and the Smagorinsky-Lilly model with a coefficient C_s of 0.1 is selected as the subgrid-scale model. The filtered equations are solved by the pressure-based implicit solver. The segregated algorithm, Semi-Implicit Method for Pressure Linked Equation-Consistent (SIMPLEC), is used for the pressure-velocity coupling. The time step of the CFD simulations is 0.01 s.

2.4 Simulation of tornado translation

In Cases 3 and 4 where the dome structure is present, a translating tornado is simulated to determine more realistic tornadic wind loads. In order to simulate the tornado translation, the dome structure is made to translate in the opposite direction to the direction of tornado translating, instead of making the tornado translate. First, the dome structure is placed at 360 m on the X axis (t = 0 s), as shown in Fig. 4. Then, the dome structure is made to move to the left (along the negative X direction) at a speed of 15 m/s, which is the translating speed of Spencer Tornado based on the field measurement data [45], simulating the translation of the tornado from the left to the right. When t = 24 s, the dome structure moves to the center of the tornado. When t = 48 s, the dome structure moves to -360 m on the X axis, and the calculation is terminated.

To fulfill the translation of the dome structure inside the computational domain, the dynamic mesh technique is applied. Zone 1 containing the dome structure in Fig. 3(b) is defined as a rigid body, which moves at the speed of 15 m/s in the negative X direction during the tornado translating. Zones 2 and 3 in Fig. 3(b) are defined as dynamic mesh zones. Layering technique is applied to the dynamic mesh zones to allow the movement of Zone 1. Zone 4 in Fig. 3(b) is defined as a stationary zone. Moreover, the boundary condition on the ground plane is defined as a moving wall with the speed of 15 m/s in the negative X direction, simulating the relative motion between the tornado and the ground plane. More details about the application of dynamic mesh can be referred to [43].

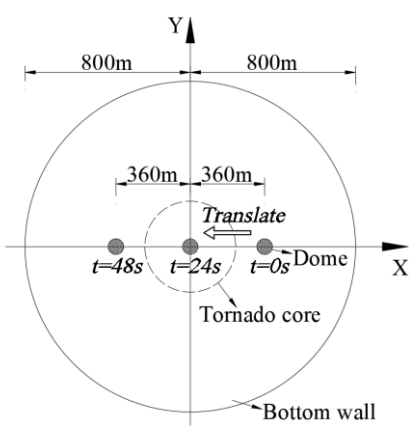


Fig. 4. Illustration of the simulated tornado translation.

3. Verification of the CFD Simulation Model

Case 1 aims to reproduce Spencer Tornado, a dual-celled tornado. To verify the applied CFD simulation strategies, the obtained simulation results are compared with the radar-measured data in terms of the tangential velocity profile (V_t) , radial Reynolds number (R_{e_r}) and swirl ratio (S), as well as the flow structure on the vertical plane.

3.1 Profile of tangential velocity (V_t)

The comparison between the simulated results and the radar-measured data is shown in Fig. 5, with respect to the averaged V_t profile as a function of radial distance at the elevation of 80 m. V_t profile at the elevation of 80 m is selected to do the comparison to eliminate the requirement of matching the ground roughness between the CFD simulation and radar measurement, assuming that the influence of ground roughness on the wind flow at the elevation of 80 m is minimal. To achieve an appropriate comparison, the averaging method applied to the simulated V_t profile is the same as the one applied to process the radarmeasured data [28]. To be specific, first, V_t along a radius on the horizontal 80-m-high plane is extracted during a period of 20 s, and then it is time-averaged. Time-averaged V_t along 36 radii are obtained. Next, the space-averaged V_t at each specified radial distance is calculated by averaging the values at the same radial distance over the 36 azimuth angles. A data regression technique is applied on the time-averaged V_t profile along each radius to ensure the data availability at the specified radial distances. A similar method was also used to obtain the averaged V_t from laboratory tornado simulations [16, 23, 46]. As shown in Fig. 5, the averaged V_t profile obtained from the CFD simulation is in general agreement with that obtained from the radar-measured data. From Fig. 5, tornado center is located at the radial distance of 0 m; and R_c of the simulated tornado is 230 m and the corresponding $V_{t,max}$ is 65 m/s. In terms of R_c and $V_{t,max}$, the simulated results match the radar-measured data very well. Some minor deviations are found within R_c and around a radial distance of 600 m. These deviations can be caused by the fixed boundary conditions and velocity input deployed in the CFD simulations, although the real-world tornado is subjected to unsteady boundary conditions. The present authors have been improving this by coupling WRF (Weather

Research Forecast) software with CFD simulation in order to introduce the variability in time and space of the velocity input. Since R_c and $V_{t,max}$ (representing the size and intensity of the tornado) are the two most important factors for determining the design tornadic wind loads, such deviations are acceptable.

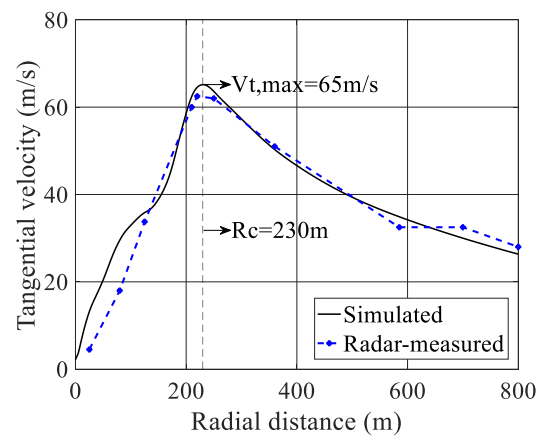
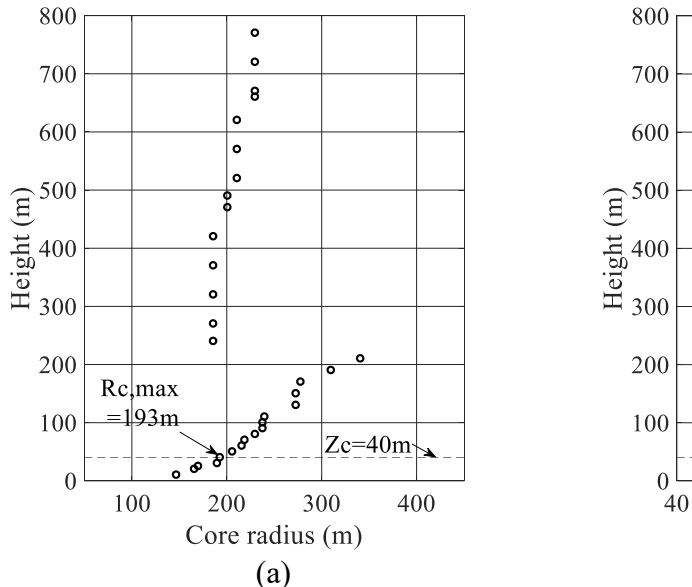


Fig. 5. Comparison of the tangential velocity profiles extracted from the CFD simulation (Case 1) and the radar-measured data.

3.2 Profiles of core radius (R_c) and maximum tangential velocity $(V_{t,max})$

The core radius (R_c) and maximum tangential velocity $(V_{t,max})$ of the simulated tornadic wind field (Case 1) as a function of height are shown in Fig. 6. From Fig. 6(a), the tornado core exhibits a cylindrical shape aloft and a conical shape close to the ground, and a discontinuity (a "bulge") emerges at the elevation around 210 m. These findings are consistent with the observations reported by Hangan and Kim for the vortex core shape with higher S [47]. From Fig. 6(b), the overall $V_{t,max} = 73.5$ m/s occurs at the height of 40 m ($z_c = 40$ m), and the corresponding core radius is 193 m ($R_{c,max} = 193$ m), which are in general agreement with the radar-measured data [23]. It should be noted that z_c is defined as the height at which the overall (absolute) maximum tangential velocity is observed.



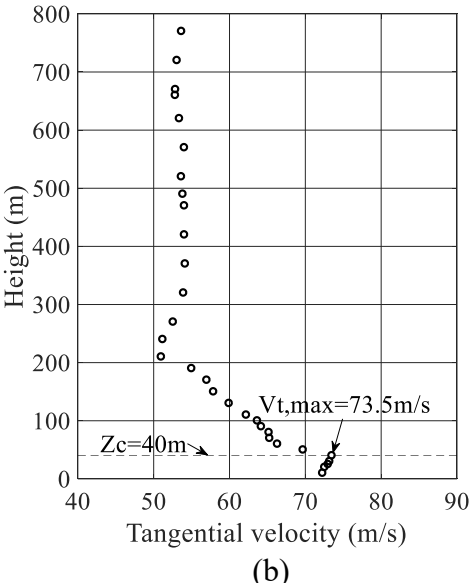


Fig. 6. Dual-celled tornado (Case 1): (a) Profile of core radius along height; (b) Profile of maximum tangential velocity along height.

3.3 Radial Reynolds number (R_{e_r}) and swirl ratio (S)

Radial Reynolds number R_{e_r} and swirl ratio (S) control the flow structure of the tornado [13]. R_{e_r} reflects the degree of flow turbulence, and it is defined as the ratio of volume flow rate per unit inflow height to flow viscosity:

$$R_{e_r} = \frac{\dot{Q}'}{2\pi\nu} = \frac{Q}{2\pi\nu h} \tag{3}$$

where Q' represents the volume flow rate per unit axial length of inflow height and Q represents the total volume flow rate through the system. Herein, $Q = 1.15 \times 10^7$ m³/s. ν denotes kinematic viscosity $(1.53 \times 10^{-5} \text{ m}^2/\text{s})$, and h denotes the height of the velocity inlet (100 m). R_{e_r} of the simulated tornado is 1.20×10^9 , which falls into the estimated range of actual tornado cyclone flows, 10^9 - 10^{11} [13].

S is essentially a measure of the relative amount of angular to radial momentum in the vortex, reflecting the amount of rotational energy in the vortex relative to the convective energy in the vortex [18]. S at a certain height is defined as [47]:

$$S = \frac{\pi R_c^2 V_{t,max}}{O} \tag{4}$$

where R_c is the core radius at that specific height, and $V_{t,max}$ is the corresponding maximum V_t (the V_t at R_c) at that height. S of the simulated tornado at seven representative heights are presented in Fig. 7. S ranges from 1 to 2 within 200 m, which is consistent with the conclusions drawn by Hangan and Kim [47].

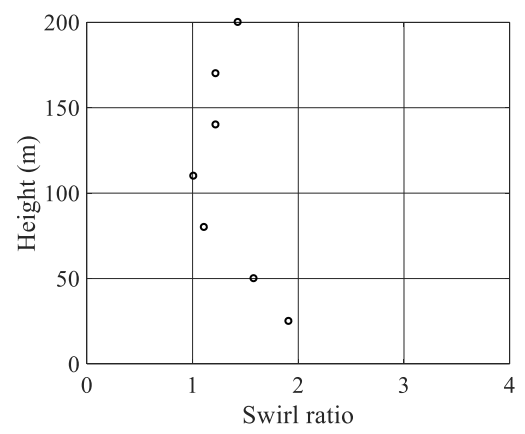


Fig. 7. Swirl ratio at representative heights for the dual-celled tornado (Case 1).

3.4 Vertical flow structure

The schematic diagrams of ideal tornadic flow structures on a vertical plane are shown in Fig. 8 [48]. Figure 8(a) presents a dual-celled single-vortex flow structure, which is formed when S is relatively high (e.g., $0.5 \le S \le 1.0$, and S is defined as $S = r_0 \Gamma/(2Q)$, where r_0 is the radius of the updraft hole, Γ is the far-field tangential circulation, Q is the total volume flow rate through the system [13]. It should be noted that the range of S is estimated from laboratory experiments, which is approximate because they depend slightly on Reynolds number and they are tornado simulator dependent because of differences in the height of the honeycomb baffle compared to r_0 [48]). A downdraft is formed at the tornado center and touches the ground surface, widening the corner flow. Figure 8(b) presents a single-celled single-vortex flow structure and it is formed when S is low (e.g., $0.1 \le S \le 0.5$ [13]). No downdraft is observed and the corner flow forms an intense lateral inflow and upward jet.

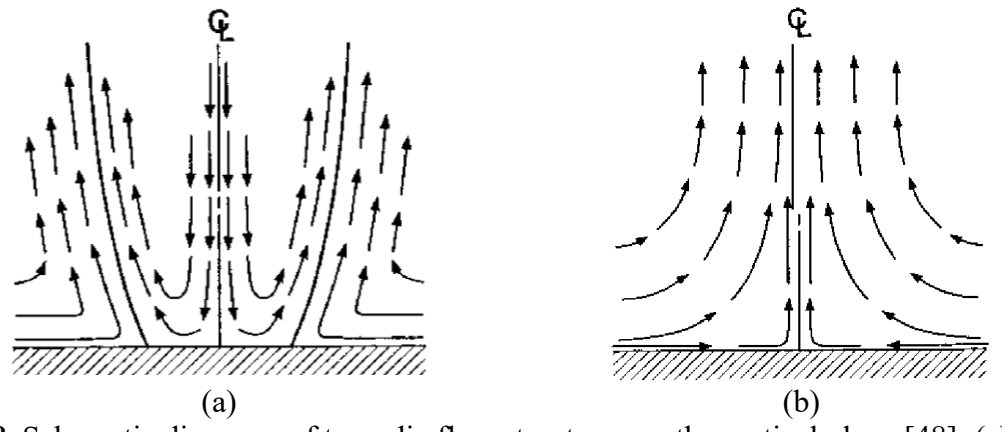


Fig. 8. Schematic diagrams of tornadic flow structures on the vertical plane [48]: (a) Dualcelled single-vortex flow structure; (b) Single-celled single-vortex flow structure.

To demonstrate a dual-celled single-vortex tornado is generated in Case 1, the 1-s averaged flow structure on the vertical plane of the simulated tornado is shown in Fig. 9(a). It is extracted from a meridional plane of the computational domain. From the flow structure on

the vertical plane, it can be seen that a downdraft is formed at the tornado center, impinging the ground, indicating a dual-celled flow structure comparing to Fig. 8(a). Such a central downdraft is a main feature of dual-celled tornadoes, as also reported by Fiedler and Rotunno [49]. Updraft is formed at the outer region. Small vortices are formed due to local turbulence of airflow. Thus far, the simulated results are in general agreement with the radar-measured data, thus validating the feasibility of the applied CFD simulation strategies. Further analyses will be conducted based on these CFD simulation strategies.

4. Comparison on Wind Characteristics of Tornadic Wind Field

In this section, the wind characteristics of tornadic wind field with the two different flow structures will be investigated. Comparisons between Cases 1 and 2 will be made regarding the flow structure, tangential velocity (V_t) , turbulence intensity (TI), and static pressure.

4.1 Tornadic flow structure

The 1-s averaged flow structures on the vertical plane of the two types of tornadoes are shown in Fig. 9. From Fig. 9, updraft is formed at the outer region of the computational domain for both cases. However, downdraft is only formed at the tornado center of the dual-celled tornado (Fig. 9(a)), while the airflow at the tornado center of the single-celled tornado is still updraft (Fig. 9(b)). This is the main difference between dual- and single-celled tornadoes regarding the flow structure on the vertical plane. Small vortices due to local turbulence are observed for both cases. In general, the flow structures of both cases match the corresponding schematic diagram of ideal tornadic flow structure (Fig. 8) well.

According to Eq. (4), S is determined as 1.63 for the dual-celled tornado at the elevation of $z_c = 40$ m (Fig. 6(b)) and 0.14 for the single-celled tornado at the elevation of $z_c = 70$ m (Fig. 14(b)). S is consistent with the research findings about the effect of increasing S on tornadic flow structure [13, 16, 25, 26, 46, 48], i.e., a dual-celled tornado is formed when S is high and a single-celled tornado is formed when S is low. Based on Eq. (3), R_{e_r} of both cases is the same, that is, 1.20×10^9 , since they share the same velocity input and dimensions at the velocity inlet.

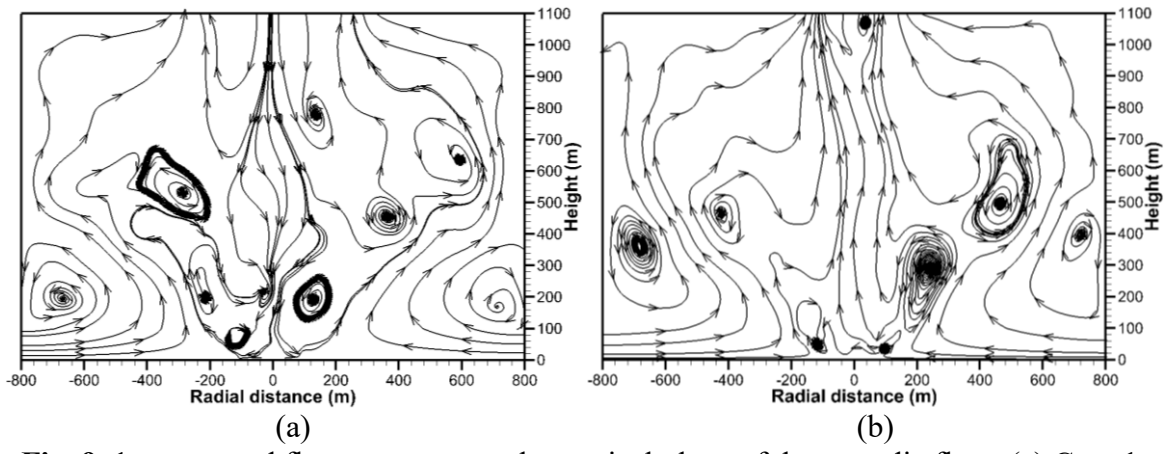


Fig. 9. 1-s averaged flow structure on the vertical plane of the tornadic flow: (a) Case 1:

The 1-s averaged flow structure on the horizontal plane at the elevation of 25 m is shown in Fig. 10. The elevation of 25 m is chosen, as this is the height of the dome apex. In both cases, the air rotates counterclockwise. From the radius where $V_{t,max}$ is reached (core radius, R_c), R_c for the dual-celled tornado (Case 1) is 160 m and that for the single-celled tornado (Case 2) is 53 m. Here, R_c is 1-s averaged result as presented in Fig. 13. As shown in Fig. 10(a), it is interesting to point out that, the outer air flows in towards R_c , and the inner air flows out towards R_c due to the centrifugal force induced by the air rotation. In other words, the airflow converges at R_c for the dual-celled tornado. For the single-celled tornado, a similar phenomenon is observed but the airflow converges at a radial distance that is 50 m away from R_c , as shown in Fig. 10(b). The convergence location of the airflow depends on the force balance between the pressure gradient force (inwards) and the centrifugal force (outwards). For the single-celled tornado (Case 2), $V_{t,max}$ is much higher (see Fig. 12), leading to a much higher centrifugal force. This is why the convergence location of the airflow is further away from R_c . Based on the flow analysis on the horizontal plane, it is worth noting that the large atmospheric pressure drop at tornado center (the maximum negative pressure) is due to the fact that the air flows outwards in the core region.

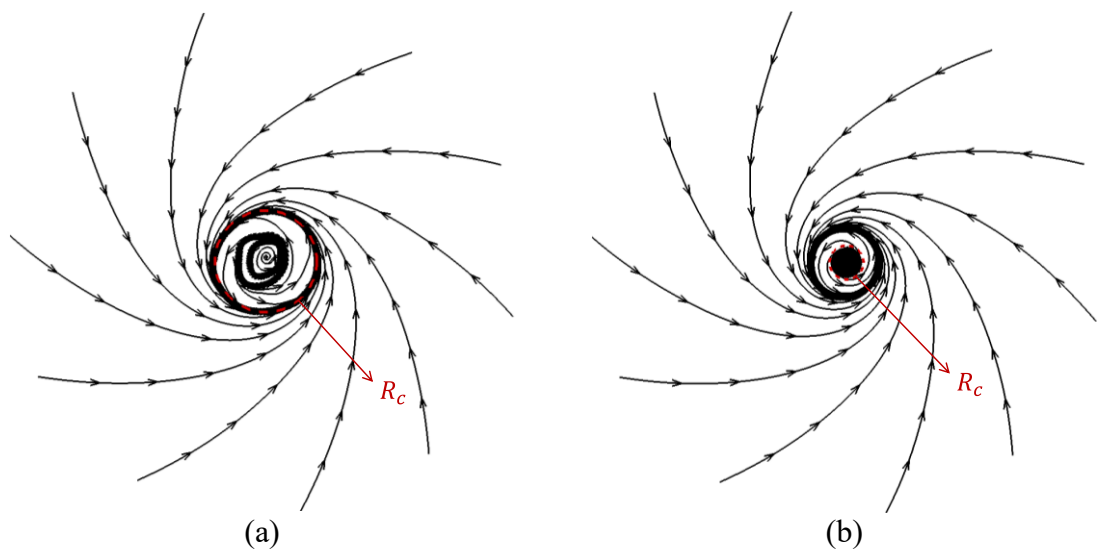


Fig. 10. 1-s averaged horizontal flow structure of the tornadic wind field at the elevation of 25 m (Note: R_c denotes the core radius in each case): (a) Case 1: Dual-celled; (b) Case 2: Single-celled.

4.2 Tangential velocity (V_t)

1-s averaged contour plots of V_t on the horizontal plane at the elevation of 25 m are shown in Fig. 11. For both cases, the distribution of V_t is in the pattern of concentric circles. R_c of the dual-celled tornado is much larger than that of the single-celled tornado. They are 160 m and 53 m, respectively, and indicated by dashed circles in Fig. 11. The maximum V_t of the single-celled tornado (190 m/s) is much larger than that of the dual-celled tornado (86

m/s), which can be qualitatively explained by the conservation of angular momentum. The minimum V_t for both cases is similar. Here, R_c and V_t are 1-s averaged results.

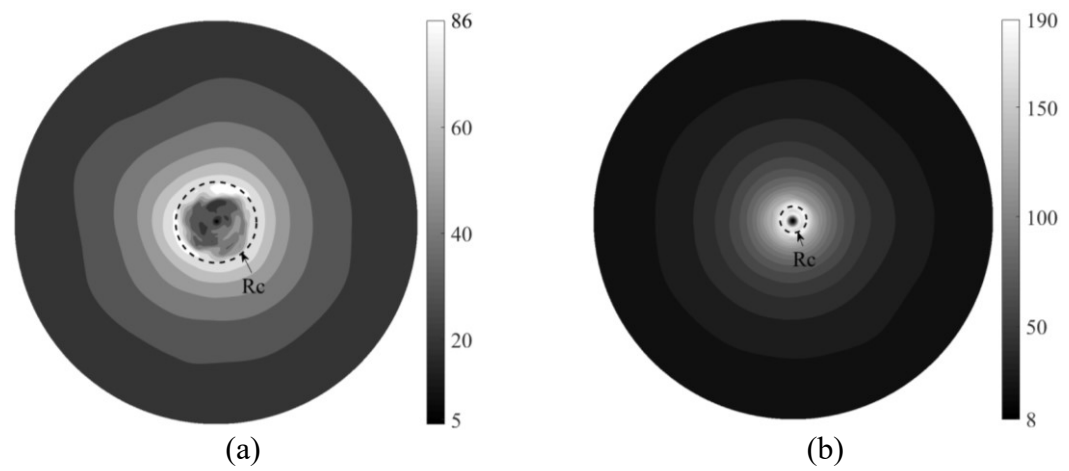


Fig. 11. 1-s averaged contour plots of tangential velocity on the horizontal plane at the elevation of 25 m (Unit: m/s): (a) Case 1: Dual-celled; (b) Case 2: Single-celled.

To be more specific, V_t profiles along one radius at the elevation of 25 m and 80 m are presented in Fig. 12. Here, V_t is time- and space-averaged. For both elevations, R_c of the dual-celled tornado is larger than that of the single-celled tornado, while $V_{t,max}$ of the dual-celled tornado is smaller. Qualitatively, this is consistent with the conservation of the angular momentum. Figure 13 presents the 1-s and space-averaged V_t profile at the elevation of 25 m for both types of tornadoes. It is in general agreement with the corresponding time- and space-averaged V_t profile.

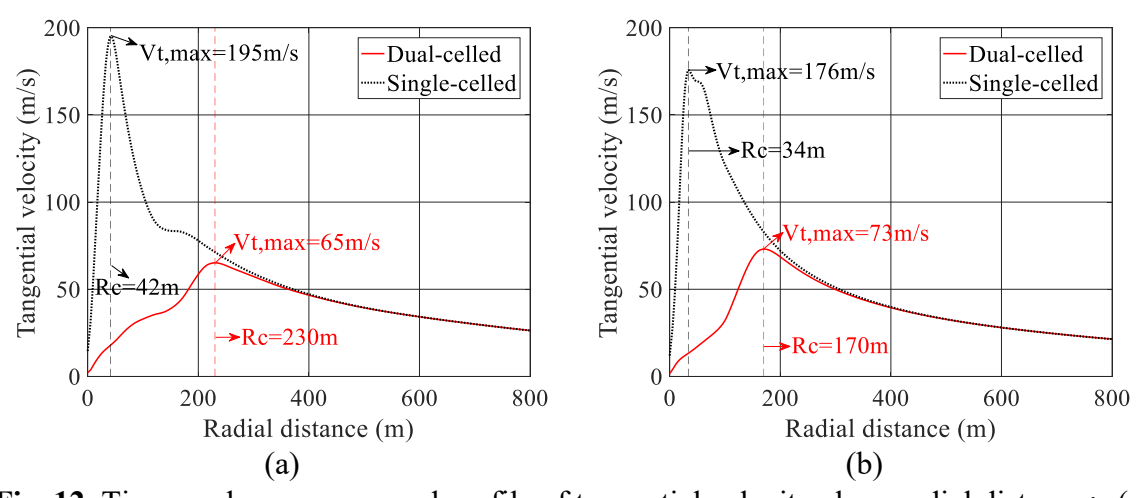


Fig. 12. Time- and space-averaged profile of tangential velocity along radial distance: (a) At the elevation of 80 m; (b) At the elevation of 25 m.

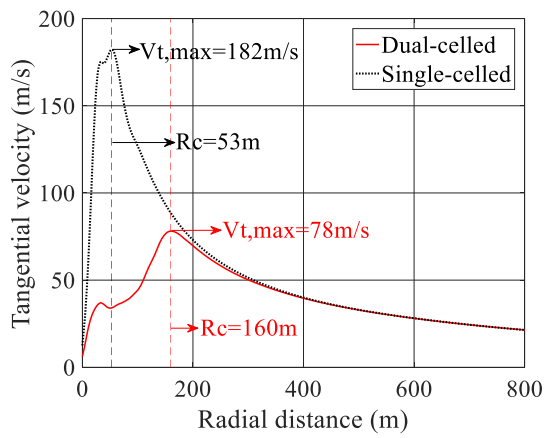


Fig. 13. 1-s and space-averaged profile of tangential velocity along radial distance at the elevation of 25 m.

The R_c and $V_{t,max}$ of the simulated single-celled tornado (Case 2) as a function of height is presented in Fig. 14. From Fig. 14(a), the tornado core shape of the single-celled tornado is similar to that of the dual-celled tornado (Fig. 6(a)), but without the "bulge", which is consistent with the observations reported by Hangan and Kim [47]. From Fig. 14(b), the overall $V_{t,max} = 195.6$ m/s occurs at the height of 70 m ($z_c = 70$ m), and the corresponding core radius is 43 m ($R_{c,max} = 43$ m).

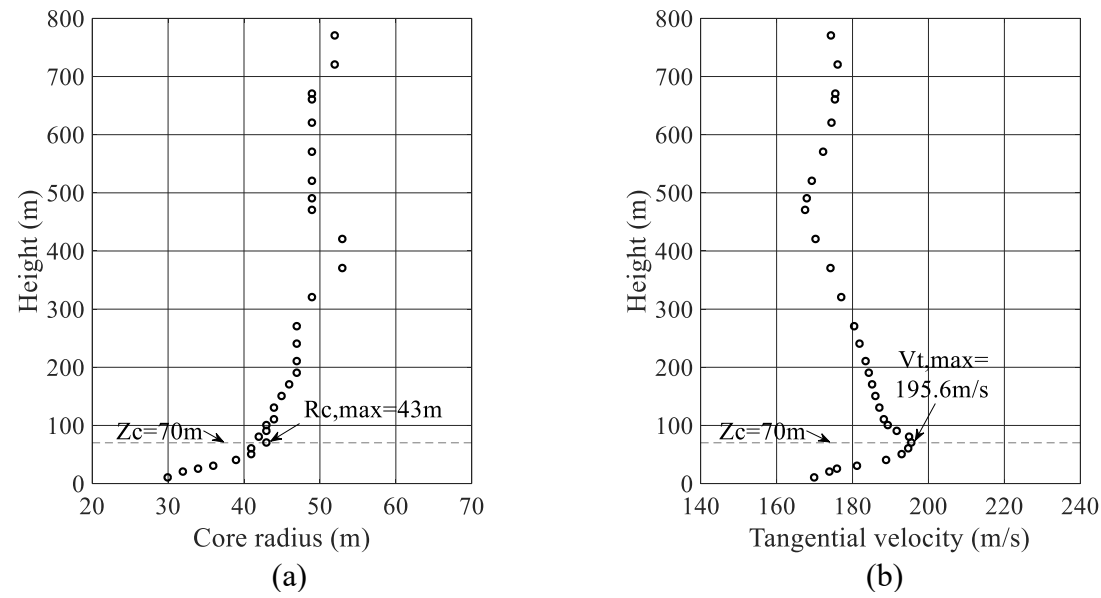


Fig. 14. Single-celled tornado (Case 2): (a) Profile of core radius along height; (b) Profile of maximum tangential velocity along height.

1-s averaged contour plots of V_t on a meridional plane is shown in Fig. 15. For lower elevations, in both cases, the distribution of V_t is symmetric about the central axis; for higher elevations, the distribution of V_t for the dual-celled tornado (Case 1) is less symmetric than that for the single-celled tornado (Case 2). This is due to the fact that there exists central downdraft and the airflow is more turbulent in the dual-celled tornado.

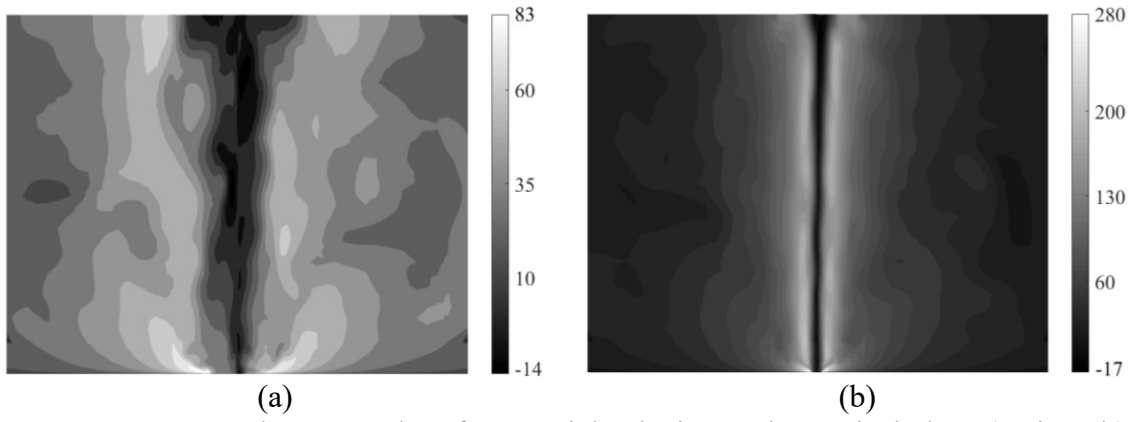


Fig. 15. 1-s averaged contour plot of tangential velocity on the vertical plane (Unit: m/s): (a) Case 1: Dual-celled; (b) Case 2: Single-celled.

4.3 Turbulence intensity (TI)

TI is used to measure the strength of turbulence, which in this study is obtained based on the time histories of wind velocity at the elevation of 25 m. TI is defined as the ratio of the root-mean-square of velocity fluctuation to the mean resultant velocity [50]. Herein the overall (absolute) maximum tangential velocity, instead of the mean resultant velocity, is used to normalize TI, in order to eliminate the singularity problem at the tornado center where the mean resultant velocity is close to zero. Eq. (5) is used to determine TI:

$$TI_u = \frac{\sigma_u}{U}, \qquad TI_v = \frac{\sigma_v}{U}, \qquad TI_w = \frac{\sigma_w}{U}$$
 (5)

where $\sigma_u^2 = \frac{1}{T} \int_0^T u^2 dt$, $\sigma_v^2 = \frac{1}{T} \int_0^T v^2 dt$, and $\sigma_w^2 = \frac{1}{T} \int_0^T w^2 dt$; u, v, and w are the velocity fluctuation in the radial, tangential and axial directions; U is the overall maximum tangential velocity of each case (U=73.5 m/s at z_c = 40 m for the dual-celled tornado (Fig. 6(b)) and U= 195.6 m/s at z_c = 70 m for the single-celled tornado (Fig. 14(b)).

Based on Eq. (5), TI at different radial distances in the axial, radial, and tangential directions for both cases are obtained and presented in Fig. 16. Radial distance is normalized using R_c of each case, i.e., 170 m for the dual-celled tornado and 34 m for the single-celled tornado (Fig. 12(b)). From Fig. 16, TI of each velocity of the dual-celled tornado is generally larger than that of the single-celled tornado, which is attributed to the presence of the central downdraft in the dual-celled tornado. This indicates that the airflow of the dual-celled tornado is more turbulent, which also demonstrates the aforementioned statement that the vertical distribution of V_t for the dual-celled tornado is less symmetric than that for the single-celled tornado at higher elevations.

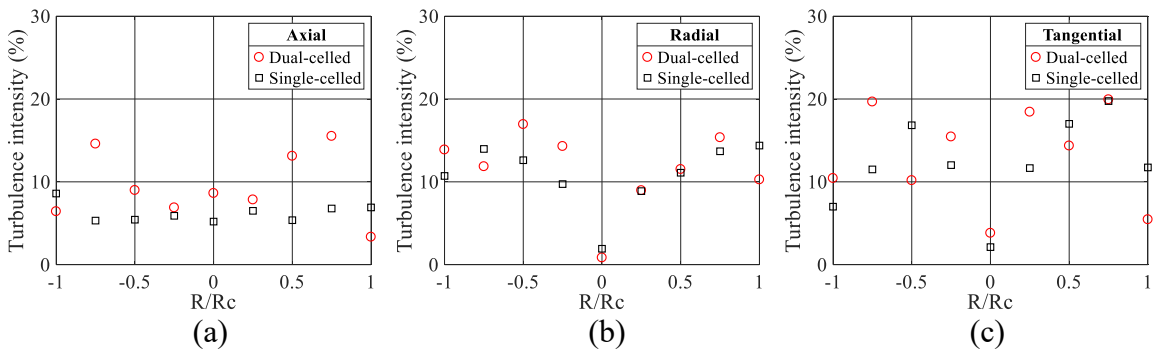


Fig. 16. Comparison of turbulence intensity between Cases 1 and 2: (a) For axial velocity; (b) For radial velocity; (c) For tangential velocity.

To demonstrate the fluctuations in velocities, the time histories of V_t for both cases at three representative locations, i.e., R_c , half of R_c and tornado center, are presented in Figs. 17-18. Both the instantaneous wind speed and its mean value are presented in each case. For both cases, the mean value decreases when the radial distance gets closer to the tornado center. At each representative radial distance, although V_t of the dual-celled tornado fluctuates less frequently than that of the single-celled tornado and the corresponding variance of the velocity data is much smaller, TI of the dual-celled tornado is higher based on Eq. (5) due to the lower mean V_t in the dual-celled tornado.

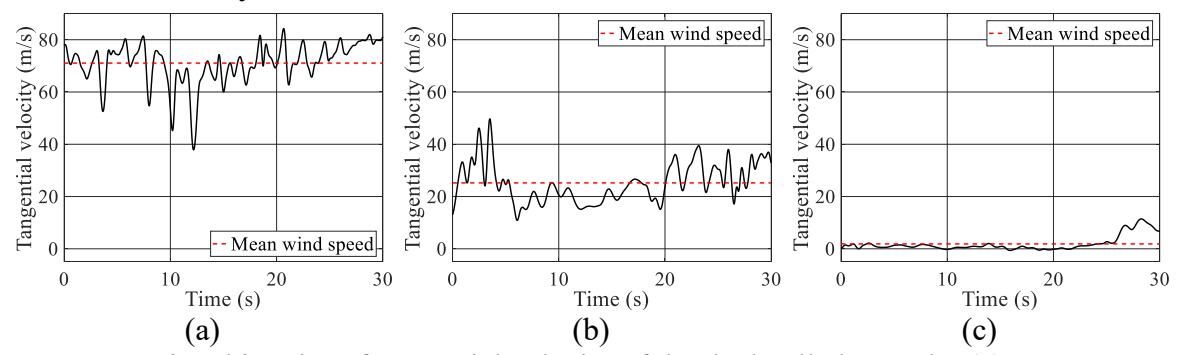


Fig. 17. Time histories of tangential velocity of the dual-celled tornado: (a) At $R=-R_c$, $\sigma_v = 7.7$; (b) At $R=-0.5R_c$, $\sigma_v = 7.5$; (c) At R=0, $\sigma_v = 2.8$ (Note: σ_v denotes the root-mean-square of tangential velocity fluctuation).

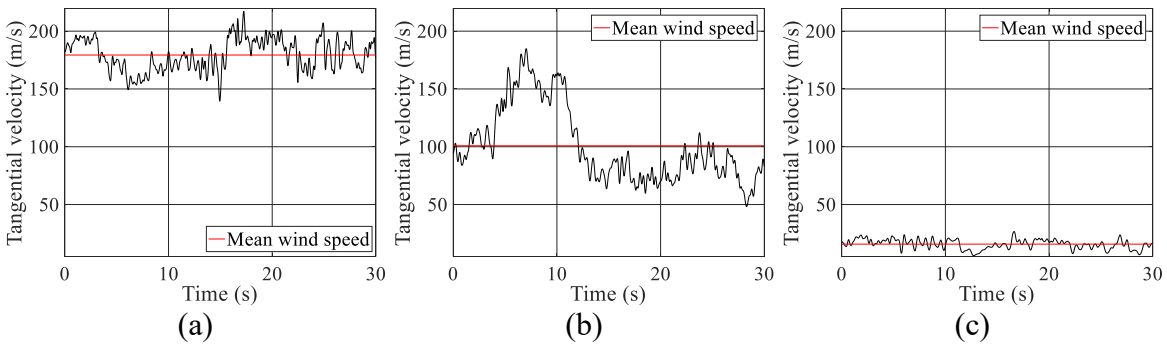


Fig. 18. Time histories of tangential velocity of the single-celled tornado: (a) At $R=-R_c$, $\sigma_v = 13.7$; (b) At $R=-0.5R_c$, $\sigma_v = 32.9$; (c) At R=0, $\sigma_v = 4.1$.

4.4 Static pressure

Figure 19 shows the 1-s averaged contour plots of static pressure coefficients on the horizontal plane at the elevation of 25 m. All pressure data are non-dimensionalized into pressure coefficients based on the reference dynamic pressure at the dome apex as

$$C_{P_i} = \frac{P_i - P_{\infty}}{\frac{1}{2}\rho V^2} \tag{6}$$

where $P_i - P_{\infty}$ represents the pressure difference between local and reference pressure P_{∞} , which is directly obtained from ANSYS FLUENT. P_{∞} is atmospheric pressure (101 kPa). ρ is the density of air (1.225 kg/m³). V is the reference mean velocity that is taken at the dome apex, which is 73 m/s for the dual-celled tornado and 176 m/s for the single-celled tornado (See Fig. 12(b)).

From Fig. 19, for both cases, the distribution of static pressure is in the pattern of concentric circles. Within the tornado core, negative pressure is present due to a high atmospheric pressure drop. Static pressure increases with the increase of radial distance. It is also observed that the distribution of negative pressure within R_c is scattered for the dual-celled tornado (Fig. 19(a)) and is centered for the single-celled tornado (Fig. 19(b)). This further verifies that the dual-celled tornado is more turbulent inside the tornado core than the single-celled tornado.

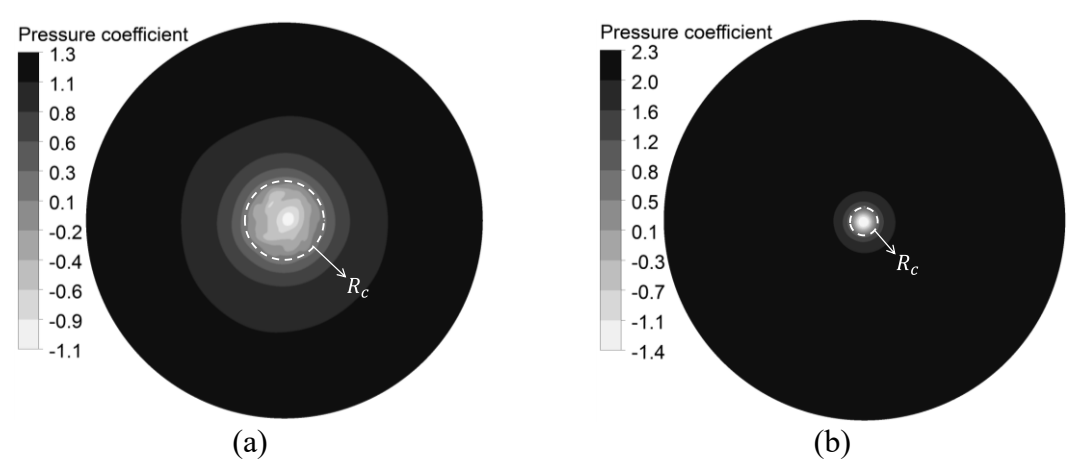


Fig. 19. 1-s averaged contour plot of static pressure coefficient on the horizontal plane at the elevation of 25 m: (a) Case 1: Dual-celled; (b) Case 2: Single-celled.

To be more specific, the profile of static pressure coefficient along a diameter of the computational domain is shown in Fig. 20. Here, static pressure coefficient is time- and space-averaged and normalized using Eq. (6). In both cases, the maximum negative pressure occurs at the tornado center, as the air flows outwards away from tornado center within the tornado core. There are three main differences between the two cases. First, the pressure gradient of the dual-celled tornado is much smaller than that of the single-celled tornado. Second, for the dual-celled tornado, the region with the maximum negative pressure is wide, while that for the single-celled tornado is narrow, exhibiting as a peak. Third, the pressure magnitude range of the dual-celled tornado is much smaller than that of the single-celled tornado. These findings

are consistent with experimental results obtained from laboratory tornado simulators [25, 51].

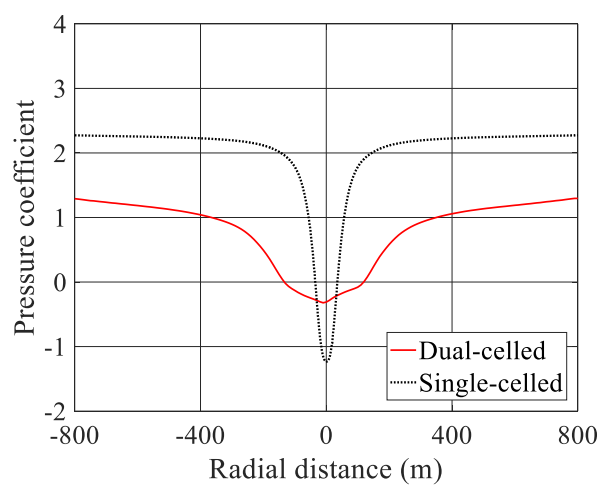


Fig. 20. Profile of static pressure coefficient along radial distance.

5. Comparison on Tornado-induced Wind Effects on the Dome Structure

In this section, tornado-induced wind effects are compared between Cases 3 and 4 when the dome structure is present in the wind field. The wind effects presented here include the wind pressure on the dome surface (hereafter "surface pressure") and total forces and moments acting on the entire dome.

5.1 Surface pressure

Figure 21 presents the surface pressure coefficients induced by the dual-celled tornado (Case 3) at six representative time instants during the movement of the dome (Fig. 4). All pressure coefficients are determined using Eq. (6), with the reference mean velocity V of 73 m/s at the dome apex (See Fig. 12(b)). In general, all surface pressures are positive when the dome is far away from the tornado center (Fig. 21(a)), while negative surface pressure is gradually developed when the dome approaches the tornado center. From Fig. 21(b), when the dome is closer to the tornado center, since it is still on the right side of the tornado center, the wind blows towards the southeast corner of the dome where the surface pressure reaches its positive peak value. In Fig. 21(c), when the R_c is reached (Here, R_c is 170 m, which is at the height of the dome apex, 25 m, and is determined from Case 1 when the dome structure is not present, see Fig. 12(b)), the wind blows from due south and the surface pressure near the south edge of the dome reaches its positive peak value. As shown in Fig. 21(d), when the tornado core exactly encloses the dome structure, relatively uniform negative pressure is developed on the dome surface, which is caused by the large atmospheric pressure drop within the tornado core (see Fig. 20). When the dome passes and moves away from the tornado center (Figs. 21(e)-(f)), the northwest corner of the dome is the windward direction where peak positive pressure is found.

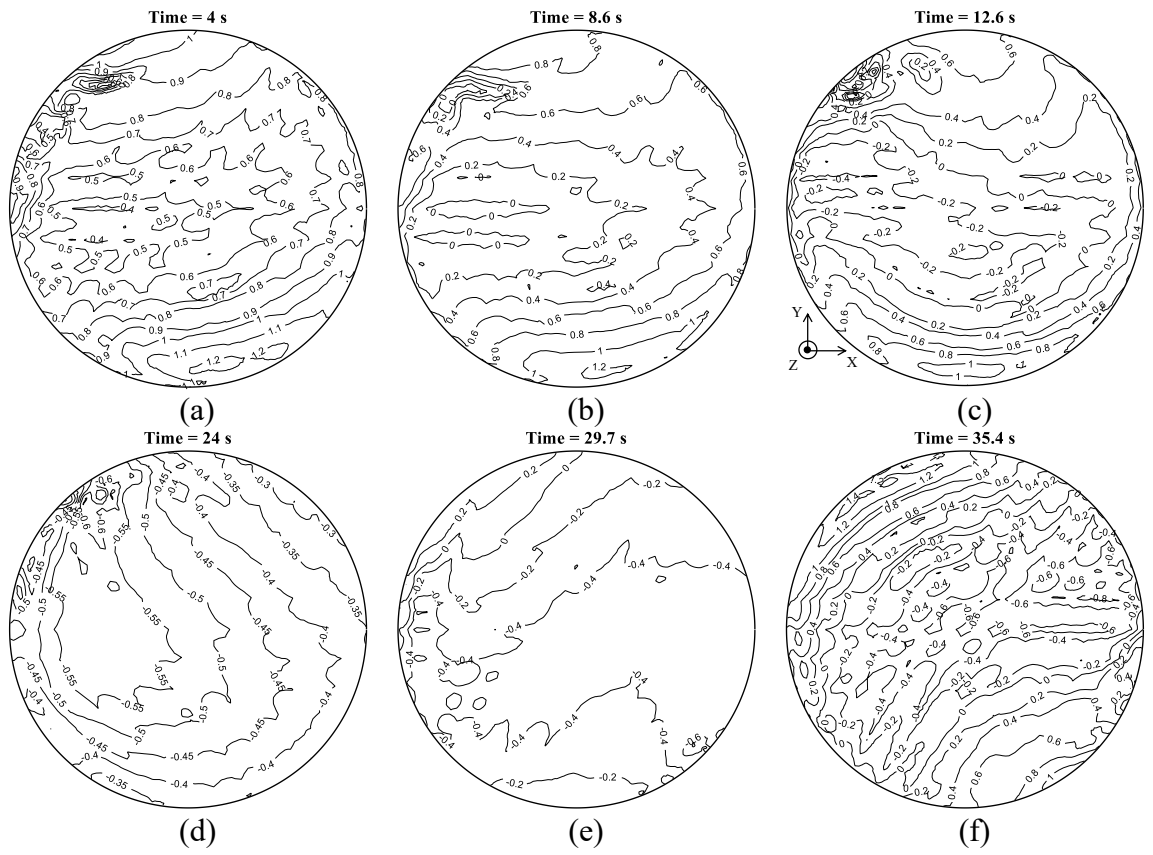


Fig. 21. Surface pressure coefficients on the dome structure for the dual-celled tornado (Case 3): (a) 4 s (300 m away from tornado center); (b) 8.6 s (231 m away from tornado center); (c) 12.6 s (171 m away from tornado center); (d) 24 s (0 m away from tornado center); (e) 29.7 s (-85.5 m away from tornado center); (f) 35.4 s (-171 m away from tornado center).

Figure 22 shows the surface pressure coefficients (the reference mean velocity is 176 m/s at the dome apex, as shown in Fig. 12(b)) induced by the single-celled tornado (Case 4). The general trend is similar to that induced by the dual-celled tornado, that is, all surface pressure is positive when the dome is far away from the tornado center, while negative surface pressure is developed when the dome gets closer to the tornado center. In this case, R_c is 34 m at the elevation of 25 m (Fig. 12(b)). By comparing Figs. 21(a) and 22(a), when the dome center is 300 m away from the tornado center, the distribution of positive surface pressure induced by the single-celled tornado is more uniform than that induced by the dual-celled tornado. This is because the tornado core of the single-celled tornado is much smaller, and the negative pressure at tornado center exerts less influence on the airflow at the 300-m radius. Therefore, the pressure gradient at the 300-m radius in the single-celled tornado is much smaller (see Figs. 23(a) and 24(a)), and thus induces less uneven distribution of surface pressure.

When the dome is at the tornado center, the distribution of surface pressure induced by the dual-celled tornado (Fig. 21(d)) is more uniform than that induced by the single-celled tornado (Fig. 22(d)). This is due to the influence of the relative size of the tornado core and the dome structure. The core diameter of the dual-celled tornado is 340 m at the elevation of 25 m, which is 4.5 times the base diameter of the dome structure (75 m). The similar ratio for

the single-celled tornado is around 0.9. This indicates that the size of the dome structure is much less than the core of the dual-celled tornado, meaning the dome structure is completely immersed in the lower pressure region. Therefore, the distribution of surface pressure is much uniform under the dual-celled tornado. The peak negative pressure coefficient on the dome is -2.0, as shown in Fig. 22(d), which is similar to the results reported by Yousef et al. [52-53]. From Figs. 21(d) and 22(d), comparison of the peak negative pressure coefficient shows that the magnitude of the pressure coefficient decreases when the tornado changes from the single-celled tornado (S=0.14) to the dual-celled tornado (S=1.63), indicating that the magnitude of the pressure coefficient decreases with S. These findings are consistent with the observations made by Cao et al. [54-55].

In addition, it is interesting to notice that a spot of localized peak negative pressure occurs in Figs. 22(c)-(e), which is indicated by dense circles. The core of the single-celled tornado is affected by the dome structure more significantly, which can be seen clearly from Figs. 23-24. For the dual-celled tornado (Fig. 23), the pressure distribution within the core is scattered, on which the influence of the dome structure is not noticeable. For the single-celled tornado (Fig. 24), when the dome structure is far away from the tornado center, the pressure is distributed in concentric circles and centered at the core. When the dome moves close to the core, the pattern of concentric circles is disturbed by the dome structure and the localized peak negative pressure coefficient is observed, i.e., Figs. 24(c)-(d). The localized peak negative pressure in Figs. 24(c)-(d) corresponds with the spot of localized peak negative pressure on the dome surface in Figs. 22(c)-(d).

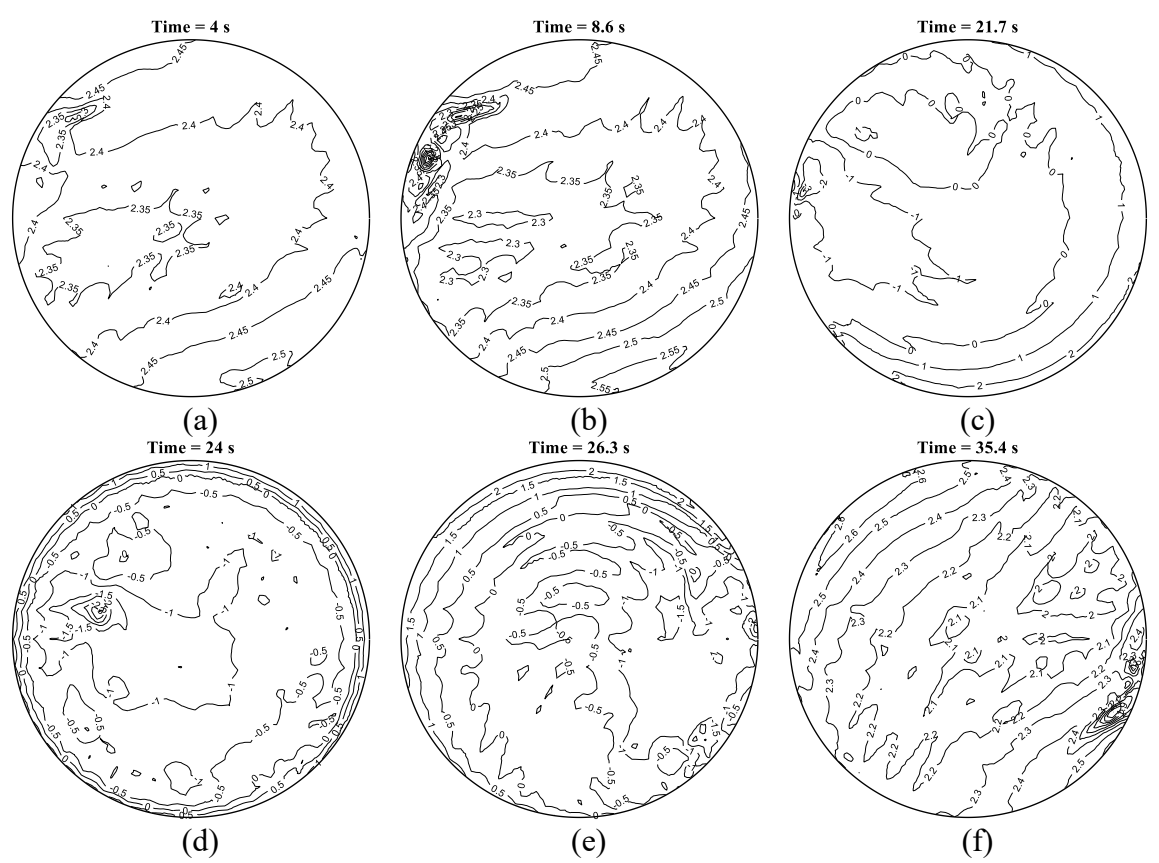


Fig. 22. Surface pressure coefficients on the dome structure for the single-celled tornado

(Case 4): (a) 4 s (300 m away from tornado center); (b) 8.6 s (231 m away from tornado center); (c) 21.7 s (34.5 m away from tornado center); (d) 24 s (0 m away from tornado center); (e) 26.3 s (-34.5 m away from tornado center); (f) 35.4 s (-171 m away from tornado center).

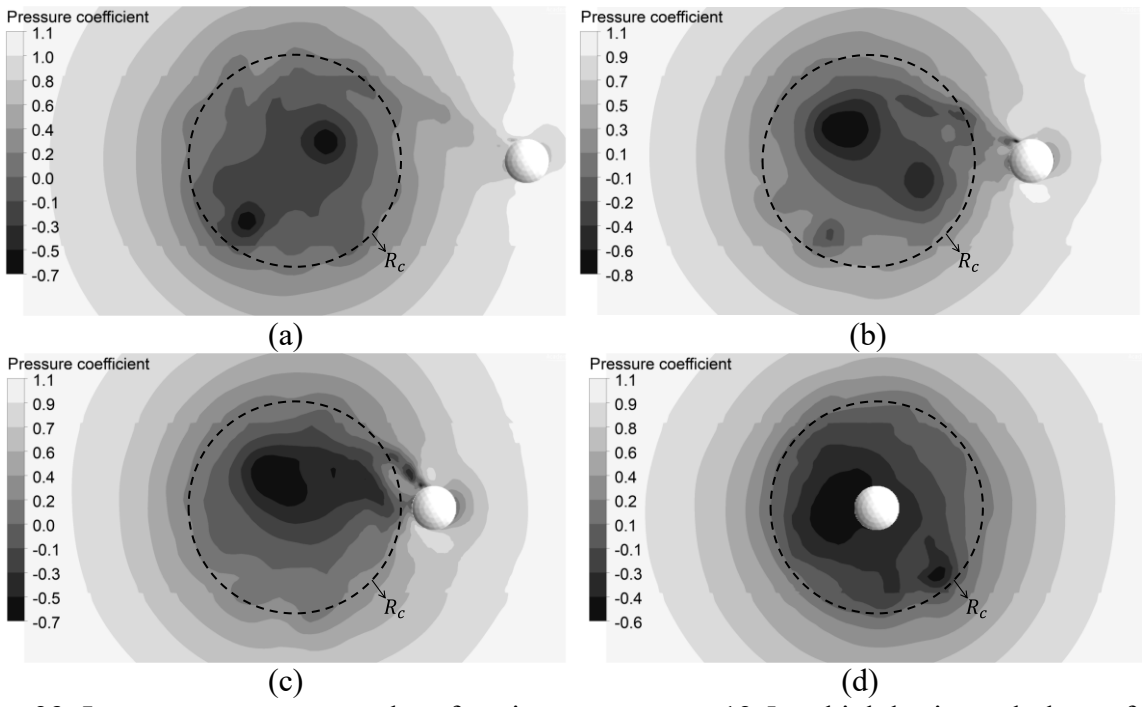
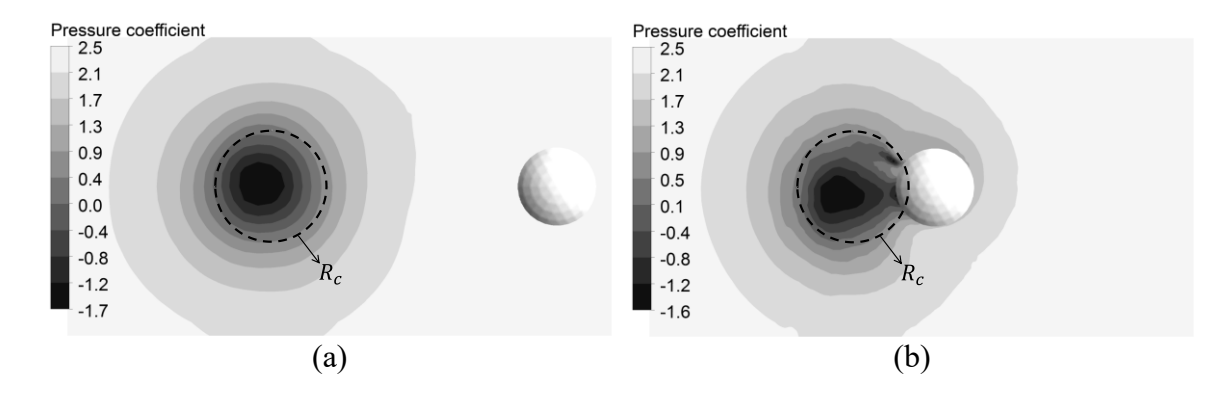


Fig. 23. Instantaneous contour plot of static pressure on a 12.5-m-high horizontal plane of the wind field induced by the dual-celled tornado (Case 3) (Note: R_c = 138 m at the elevation of 12.5 m at the time instant when the dome starts to move): (a) Dome center is 300 m away from tornado center; (b) Dome center is 210 m away from tornado center; (c) Dome center is 180 m away from tornado center; (d) Dome center is at tornado center.



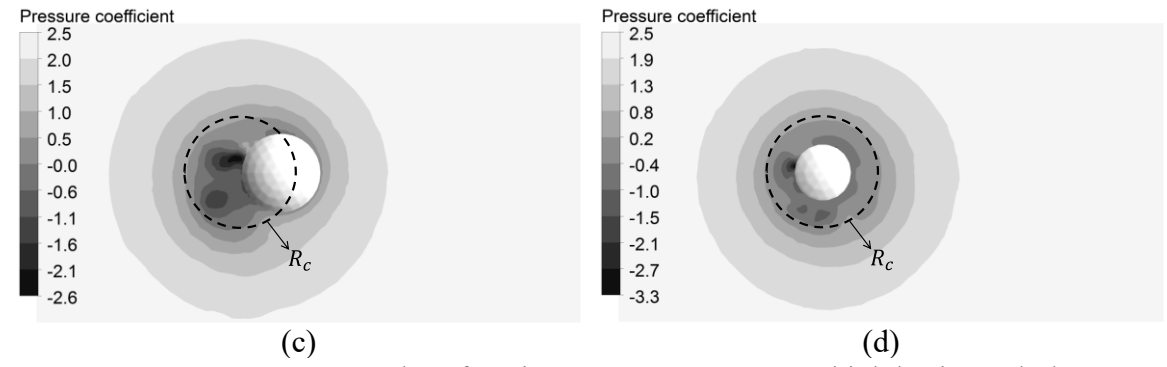


Fig. 24. Instantaneous contour plot of static pressure on a 12.5-m-high horizontal plane (except as otherwise specified) of the wind field induced by the single-celled tornado (Case 4) (Note: R_c = 41.5 m at the elevation of 12.5 m at the time instant when the dome starts to move): (a) 210 m away from tornado center; (b) 60 m away from tornado center; (c) 30 m away from tornado center; (d) At tornado center at the elevation of 19 m.

Figures 25 and 26 present the time histories of surface pressure coefficient at the dome apex from the two cases, as well as their Fourier transform (FT) and short-time Fourier transform (STFT), in order to investigate the dynamic characteristics of the surface pressure. Comparison of Figs. 25(a) and 26(a) indicates that, under both types of tornadoes, positive surface pressure is developed when the dome is far away from the tornado center and negative pressure is developed when the dome is around the tornado center because of the central atmospheric pressure drop (Fig. 20). Comparing Figs. 25(b) and 26(b), it is found that dominate frequency components in the frequency spectrum under both cases are relatively low (lower than 0.15 Hz). Figures 25(c) and 26(c) indicate the frequency variation over time for both cases. The time-frequency scalogram shows that, when the dome structure approaches and passes R_c , time variation of the surface pressure is more frequent, indicated by the presence of the higher frequency components at R_c (up to 3.75 Hz for the dual-celled tornado and 2.5 Hz for the single-celled tornado). In general, the main frequency components of the surface pressure coefficient are smaller than 0.5 Hz throughout the observation period.

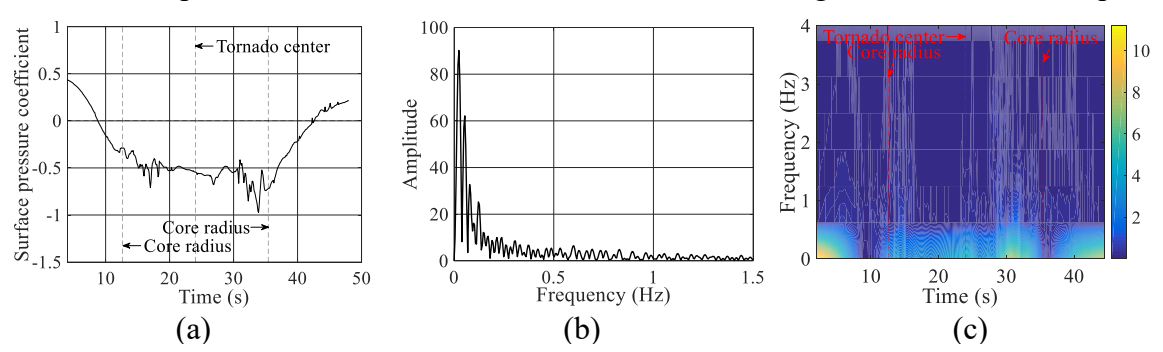


Fig. 25. Time history of the surface pressure coefficient at the dome apex induced by the dual-celled tornado (Case 3): (a) Time history; (b) Fourier transform; (c) Short-time Fourier transform.

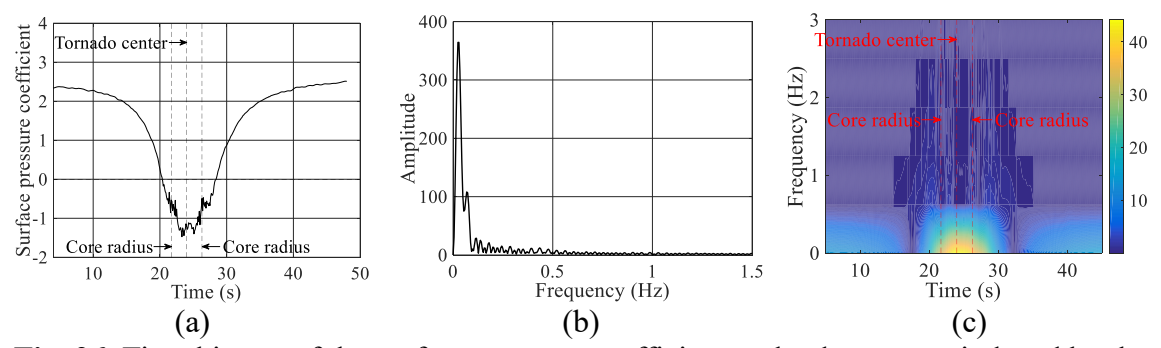


Fig. 26. Time history of the surface pressure coefficient at the dome apex induced by the single-celled tornado (Case 4): (a) Time history; (b) Fourier transform; (c) Short-time Fourier transform.

5.2 Force and moment coefficients

The wind force and moment are used to quantify the total wind effects of the tornado on the entire dome structure, which are determined by integrating the surface pressure. The total moment is taking about the center of the dome structure at the elevation of 0 m. The associated force and moment coefficients are calculated based on Eqs. (7)-(8) and presented in Figs. 27 and 28.

$$C_{F_i} = \frac{F_i}{\frac{1}{2}\rho V_{t,max}^2 A} \tag{7}$$

$$C_{F_i} = \frac{F_i}{\frac{1}{2}\rho V_{t,max}^2 A}$$

$$C_{M_i} = \frac{M_i}{\frac{1}{2}\rho V_{t,max}^2 AH}$$

$$(8)$$

where F_i and M_i are the force and moment applied on the dome structure in the i (x, y or z) direction, respectively; ρ is the density of air (1.225 kg/m^3) ; A is the projected area of the dome structure on a plane normal to the translating direction (1355 m²); H is the height of the dome structure (25 m); in each case, the reference velocity is taken as the maximum V_t at the elevation of 25 m in its own wind field, expressed as $V_{t,max}$ (73 m/s for the dual-celled tornado and 176 m/s for the single-celled tornado, see Fig. 12(b)).

From Fig. 27, when the tornado translates over the dome, the suction force (F_z) is the most significant among the three forces for both cases. This is why the roof is often seen to be torn off during tornado incidents. Fz first increases and reaches its maximum value at the tornado center, and then decreases.

For the single-celled tornado, F_x reaches its peak values when the dome moves to the tornado R_c . F_x changes its direction approximately when the dome center passes the tornado center. Since this direction change of the wind force happens very quickly in tornadic wind fields (at the tornado center), within the range of a couple of seconds, it may cause dynamic responses of the structure. It is the same case for F_{ν} induced by the single-celled tornado. However, for the dual-celled tornado, the magnitudes of F_x and F_y are much smaller than F_z , and their developments with time are more fluctuating. This is due to the scattered distribution of static pressure (Fig. 19(a)) within the larger tornado core of the dual-celled tornado. The findings about the force induced by the single-celled tornado are consistent with

laboratory tornado simulations conducted by Haan et al. [31], Hu et al. [32], Cao et al. [54], and Wang et al. [56] and numerical simulations conducted by Yousef and Selvam [57].

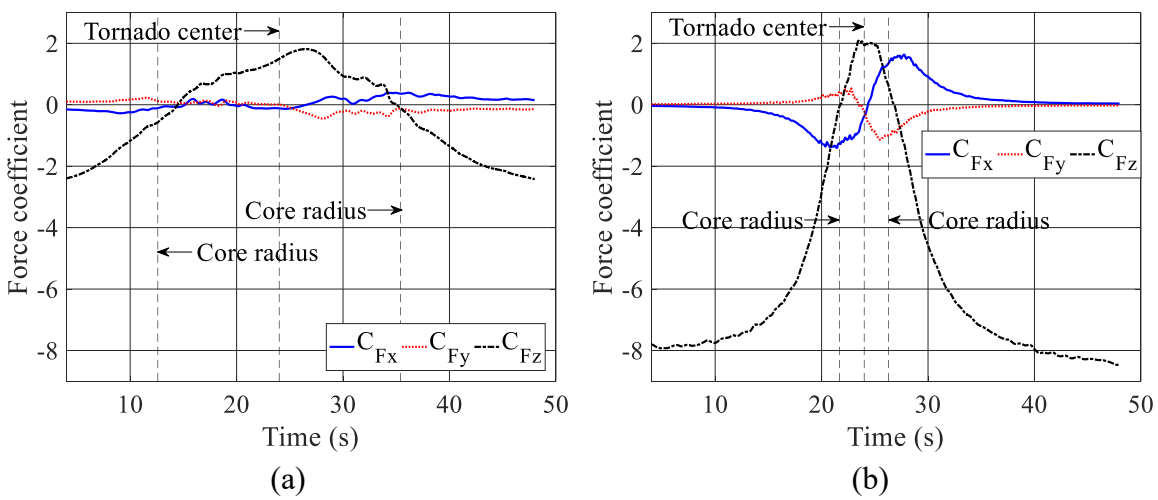


Fig. 27. Force coefficients: (a) Case 3: Dual-celled; (b) Case 4: Single-celled.

Figure 28 presents the moment coefficients acting on the entire dome structure for Cases 3 and 4. For both cases, the rotational moment (M_z) about the Z axis is very small, this is due to the fact that the geometry of the dome structure is symmetric and that the distribution of surface pressure is approximately symmetric, e.g., the surface pressure is symmetric about the Y axis in Fig. 21(c). The development of moments induced by the dual-celled tornado is more fluctuating than that induced by the single-celled tornado. The peak moments induced by the dual-celled tornado are much smaller than those induced by the single-celled tornado. For the single-celled tornado, the moment about the Y axis (M_y) is much greater than those about the other two axes, and it reaches its peak values when the dome center is about at the edge of R_c . This is because F_x is much greater. That is to say, the effect of the tornado sucking the dome towards its center is much stronger. The trends of the moments induced by the single-celled tornado are consistent with those obtained from laboratory tornado simulations conducted by Haan et al. [31] and Hu et al. [32]. This suggests that the wind loading induced by the dual-celled tornado is more dynamic than that induced by the single-celled tornado.

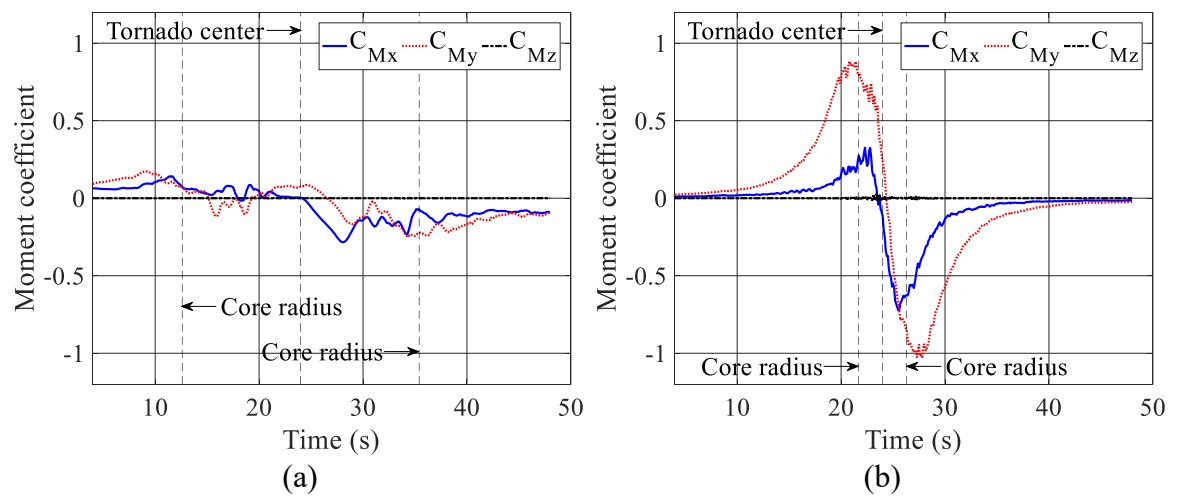


Fig. 28. Moment coefficients: (a) Case 3: Dual-celled; (b) Case 4: Single-celled.

6. Conclusions

In this study, the differences between single- and dual-celled tornadoes have been systematically investigated using CFD simulations, in respect to both the wind characteristics of tornadic wind fields and the induced wind effects on civil structures. The following conclusions can be drawn:

- The tangential velocity profile and the flow structure on the vertical plane extracted from the simulated tornadic wind field agree well with those extracted from the radar-measured data during Spencer Tornado, which demonstrates the appropriate setup for the CFD simulations.
- A dual-celled tornado is formed with a high swirl ratio, while a single-celled tornado is formed with a low swirl ratio; a touching-down downdraft is observed in the central region of the dual-celled tornado, while no downdraft is observed in the single-celled tornado; the core radius of the single-celled tornado is much smaller compared to that of the dual-celled tornado while its maximum tangential velocity is much larger, when the velocity input at the velocity inlet is the same; the pressure profile of the single-celled tornado have a narrow, single peak with a higher pressure gradient, but the corresponding profile for the dual-celled tornado has a wide, flat distribution.
- Due to the central downdraft, the turbulence intensity of the dual-celled tornado is generally higher than that of the single-celled tornado. Also, the turbulence intensities of the three velocity components are almost equivalent.
- The force and moment induced by the dual-celled tornado is more fluctuating and random than those induced by the single-celled tornado, which is caused by the presence of the central downdraft. This suggests that the wind loading induced by the dual-celled tornado is more dynamic than that induced by the single-celled tornado.
- The two drag forces $(F_x \text{ and } F_y)$ under the single-celled tornado follow a typical trend: 1) they reach their peak values when the dome center moves to the tornado core radius; 2) they change their direction approximately when the dome center passes the tornado

center; and 3) F_x is much greater than F_y , indicating that the effect of the tornado sucking the dome towards its center is much stronger. However, the corresponding variations under the dual-celled tornado tend to be more random, and the effect of sucking the civil structure towards the tornado center is not obvious. Similar observations can be found from the two overturning moments (M_x and M_y).

Acknowledgements

This work was supported by National Science Foundation, the Hazard Mitigation and Structural Engineering program, through the project of "Damage and Instability Detection of Civil Large-scale Space Structures under Operational and Multi-hazard Environments" [award number 1455709]. The authors also want to thank Mr. Jianxun Zhao, a Ph.D. student in the Department of Mechanical Engineering, for his valuable input on efficient CFD simulation setup.

References

- [1] Fujita, T.T. (1976), "Recent concept of tornado winds", *Proceedings of the 2nd USA–Japan Research Seminar on Wind Effects on Structures*, University of Tokyo, Tokyo, Japan.
- [2] Simmons, K.M. and Sutter, D. (2005), "WSR-88D radar, Tornado warnings, and tornado casualties", *Weather and Forecasting*, **20**(3), 301-310.
- [3] Rankine, W.J.M. (1858), "Manual of applied mechanics", C. Griffen Co., London, England.
- [4] Deppermann, C.E. (1947), "Notes on the origin and structure of Philippine typhoons", Bulletin of the American Meteorological Society, **28**, 399-404.
- [5] Burgers, J.M. (1948), "A mathematical model illustrating the theory of turbulence", *Advances in Applied Mechanics*, **1**, 171-199.
- [6] Rott, N. (1958), "On the viscous core of a line vortex", Zeitschrift für angewandte Mathematik und Physik ZAMP, 9(5-6), 543-553.
- [7] Sullivan, R. (1959), "A Two-cell Vortex Solution of the Navier-Stokes Equations", *Journal of Aerospace Sciences*, **26**, 767-768.
- [8] Vatistas, G.H. (1998), "New Model for Intense Self-Similar Vortices", *Journal of Propulsion and Power*, **14**(4), 462-469.
- [9] Wood V.T. and Brown R.A. (2011), "Simulated tornadic vortex signatures of tornadolike vortices having one-and two-celled structures", *Journal of Applied Meteorology* and Climatology, **50**(11), 2338-42.
- [10] Manikis, F.I. (2015), "New solutions for two-cell vortices", Thesis, Concordia University, Montreal, Quebec, Canada.
- [11] Ward, N.B. (1972), "The exploration of certain features of tornado dynamics using a

- laboratory model", Journal of the Atmospheric Sciences, 29(6), 1194-1204.
- [12] Church, C.R., Snow, J.T. and Agee, E.M. (1977), "Tornado vortex simulation at Purdue University", *Bulletin of the American Meteorological Society*, **58**(9), 900-908.
- [13] Church, C.R., Snow, J.T., Baker, G.L. and Agee, E.M. (1979), "Characteristics of tornado-like vortices as a function of swirl ratio: A laboratory investigation", *Journal of the Atmospheric Sciences*, **36**(9), 1755-1776.
- [14] Diamond, C.J. and Wilkins, E.M. (1984), "Translation effects on simulated tornadoes", *Journal of the atmospheric sciences*, **41**(17), 2574-2580.
- [15] Leslie, F.W. (1977), "Surface roughness effects on suction vortex formation: A laboratory simulation", *Journal of the Atmospheric Sciences*, **34**(7), 1022-1027.
- [16] Tari, P.H., Gurka, R. and Hangan, H. (2010), "Experimental investigation of tornado-like vortex dynamics with swirl ratio: The mean and turbulent flow fields", *Journal of Wind Engineering and Industrial Aerodynamics*, **98**(12), 936-944.
- [17] Wang, H., James, D., Letchford, C., Peterson R. and Snow, J. (2001), "Development of a Prototype Tornado Simulator for the Assessment of Fluid-Structure Interaction", *Proceedings of the 1st Americas Conference on Wind Engineering*, June 4-6, Clemson Uni., SC.
- [18] Haan, F.L., Sarkar, P.P. and Gallus, W.A. (2008), "Design, construction and performance of a large tornado simulator for wind engineering applications", *Engineering Structures*, **30**(4), 1146-1159.
- [19] Hangan, H. (2014), "The wind engineering energy and environment (WindEEE) dome at western university, Canada", *Wind Engineers*, JAWE, **39**(4), 350-351.
- [20] Haan, F.L., Sarkar, P.P., Kopp, G.A. and Stedman, D.A. (2017), "Critical wind speeds for tornado-induced vehicle movements", *Journal of Wind Engineering and Industrial Aerodynamics*, **168**, 1-8.
- [21] Razavi, A. and Sarkar, P.P. (2018), "Laboratory investigation of the effects of translation on the near-ground tornado flow field", *Wind and Structures*, **26**(3), 179-190.
- [22] Razavi, A. and Sarkar, P.P. (2018), "Laboratory study of topographic effects on the near-surface tornado flow field", *Boundary-Layer Meteorology*, 1-24.
- [23] Refan, M., Hangan, H. and Wurman, J. (2014), "Reproducing tornados in laboratory using proper scaling", *Journal of Wind Engineering and Industrial Aerodynamics*. **135**, 136-148.
- [24] Tang, Z., Zuo, D., James, D., Eguchi, Y. and Hattori, Y. (2018), "Effects of aspect ratio on laboratory simulation of tornado-like vortices", *Wind and Structures*, **27**(2), 111-121.
- [25] Tang, Z., Feng, C., Wu, L., Zuo, D. and James, D.L. (2018), "Characteristics of tornado-like vortices simulated in a large-scale Ward-type simulator", *Boundary-Layer Meteorology*, **166**(2), 327-350.
- [26] Ishihara, T., Oh, S. and Tokuyama, Y. (2011), "Numerical study on flow fields of tornado-like vortices using the LES turbulence model", *Journal of Wind Engineering*

- and Industrial Aerodynamics, 99(4), 239-248.
- [27] Ishihara, T. and Liu, Z. (2014), "Numerical study on dynamics of a tornado-like vortex with touching down by using the LES turbulence model," *Wind and Structures*, **19**(1), 89-111.
- [28] Kuai, L., Haan, F.L., Gallus, W.A. and Sarkar, P.P. (2008), "CFD simulations of the flow field of a laboratory-simulated tornado for parameter sensitivity studies and comparison with field measurements", *Wind and Structures*, **11**(2), 75-96.
- [29] Natarajan, D. (2011), "Numerical simulation of tornado-like vortices", Ph.D. Dissertation, the University of Western Ontario, London, Ontario, Canada.
- [30] Yuan, F., Yan, G., Honerkamp, R. and Isaac, K.M. (2017), "Numerical Simulation of Laboratory Tornado Simulator that can Produce Translating Tornadoes", *Journal of Wind Engineering and Industrial Aerodynamics*. Under review.
- [31] Haan, F.L., Balaramudu, V. K. and Sarkar, P.P. (2009), "Tornado-induced wind loads on a low-rise building", *Journal of Structural Engineering*, **136**(1), 106-116.
- [32] Hu, H., Yang, Z., Sarkar, P. and Haan, F. (2011), "Characterization of the wind loads and flow fields around a gable-roof building model in tornado-like winds", *Experiments in Fluids*, **51**(3), 835-851.
- [33] Mishra, A.R., James, D.L. and Letchford, C.W. (2008), "Physical simulation of a single-celled tornado-like vortex, Part B: Wind loading on a cubical model", *Journal of Wind Engineering and Industrial Aerodynamics*, **96**(8), 1258-1273.
- [34] Natarajan, D. and Hangan, H. (2012), "Large eddy simulations of translation and surface roughness effects on tornado-like vortices", *Journal of Wind Engineering and Industrial Aerodynamics*, **104**, 577-584.
- [35] Rajasekharan, S.G., Matsui, M. and Tamura, Y. (2013), "Characteristics of internal pressures and net local roof wind forces on a building exposed to a tornado-like vortex", *Journal of Wind Engineering and Industrial Aerodynamics*, **112**, 52-57.
- [36] Selvam, R.P. and Millett, P.C. (2003), "Computer modeling of tornado forces on a cubic building using large eddy simulation," *J. Ark. Acad. Sci*, **57**, 140-146.
- [37] Feng, C. and Chen, X. (2018), "Characterization of translating tornado-induced pressures and responses of a low-rise building frame based on measurement data", *Engineering Structures*, **174**, 495-508.
- [38] Sengupta, A., Haan, F. L., Sarkar, P. P. and Balaramudu, V. (2008), "Transient loads on buildings in microburst and tornado winds", *Journal of Wind Engineering and Industrial Aerodynamics*, **96**(10), 2173-2187.
- [39] Selvam, R.P. and Millett, P.C. (2005), "Large eddy simulation of the tornado-structure interaction to determine structural loadings", *Wind and Structures*, **8**(1), 49-60.
- [40] Razavi, A. and Sarkar, P.P. (2018), "Tornado-induced wind loads on a low-rise building: Influence of swirl ratio, translation speed and building parameters", *Engineering Structures*, **167**, 1-12.

- [41] Kosiba, K. and Wurman, J. (2010), "The three-dimensional axisymmetric wind field structure of the Spencer, South Dakota, 1998 tornado", *Journal of the Atmospheric Sciences*, **67**(9), 3074-3083.
- [42] Refan, M., Hangan, H., Wurman, J. and Kosiba, K. (2017). "Doppler radar-derived wind field of five tornado events with application to engineering simulations", *Engineering Structures*, **148**, 509-521.
- [43] Li, T., Yan, G., Yuan, F. and Chen, G. (2019), "Dynamic structural responses of long-span dome structures induced by tornadoes", *Journal of Wind Engineering and Industrial Aerodynamics*, **190**, 293-308.
- [44] Pointwise. (2018), V18.0 Release 3, Pointwise, Inc., Fort Worth, TX, USA.
- [45] Wurman, J. and Alexander, C.R. (2005), "The 30 May 1998 Spencer, South Dakota, storm. Part II: Comparison of observed damage and radar-derived winds in the tornadoes", *Monthly weather review*, **133**(1), 97-119.
- [46] Refan, M. (2014), "Physical Simulation of Tornado-Like Vortices", Ph.D. Thesis, the University of Western Ontario, London, Ontario, Canada.
- [47] Hangan, H. and Kim, J.D. (2008), "Swirl ratio effects on tornado vortices in relation to the Fujita scale", *Wind and Structures*, **11**(4), 291-302.
- [48] Davies-Jones, R., Trapp, R.J. and Bluestein, H.B. (2001), "Tornadoes and tornadic storms", *Proceedings of Severe convective storms*. American Meteorological Society, Boston, MA, 167-221.
- [49] Fiedler, B.H. and Rotunno, R. (1986), "A theory for the maximum wind speeds in tornado-like vortices", *Journal of the Atmospheric Sciences*, **43**(21), 2328-2340.
- [50] Tamura, Y. and Kareem, A. ed. (2015), *Advanced Structural Wind Engineering*, Springer, Japan.
- [51] Snow, J.T., Church, C.R. and Barnhart, B.J. (1980), "An investigation of the surface pressure fields beneath simulated tornado cyclones", *Journal of the Atmospheric Sciences*, **37**(5), 1013-1026.
- [52] Yousef, M. A. and Selvam, P. R. (2016), "Effect of equivalent height, surface area and volume of the dome to prism on tornado forces using CFD", *Proceedings of the 8th International Colloquium on Bluff Body Aerodynamics and Applications*, June 7-11, Northeastern University, Boston, MA, USA.
- [53] Yousef, M. A., Selvam, P. R. and Prakash, J. (2018), "A comparison of the forces on dome and prism for straight and tornadic wind using CFD model", *Wind and Structures*, **26**(6), 369-382.
- [54] Cao, S., Wang, J., Cao, J., Zhao, L. and Chen, X. (2015), "Experimental study of wind pressures acting on a cooling tower exposed to stationary tornado-like vortices", *Journal of Wind Engineering and Industrial Aerodynamics*, **145**, 75-86.
- [55] Cao, S., Wang, J. and Cao, J. (2016), "Characteristics of wind pressures on a cooling tower exposed to stationary and translating tornadoes with swirl ratio 0.54. *Journal of*

- Applied Science and Engineering, 19(3), 285-292.
- [56] Wang, J., Cao, S., Pang, W., Cao, J. and Zhao, L. (2016), "Wind-load characteristics of a cooling tower exposed to a translating tornado-like vortex", *Journal of Wind Engineering and Industrial Aerodynamics*, **158**, 26-36.
- [57] Yousef, M. A. and Selvam, P. R. (2017), "The influence of tangential to translational velocity ratio on tornado force coefficients on building using CFD", *Proceedings of the 13th Americas Conference on Wind Engineering*, May 21-24, Gainesville, Florida, USA.